Redox Biology 81 (2025) 103553

Contents lists available at ScienceDirect

Redox Biology

journal homepage: www.elsevier.com/locate/redox

Histone lactylation drives liver cancer metastasis by facilitating NSF1-mediated ferroptosis resistance after microwave ablation

Jiayan Huang [a,1], Huijing Xie [b,1], Ju Li [c,1], Xiaotong Huang [a,1], Yunshi Cai [e,f,1], Rui Yang [a], Dongmei Yang [a], Wuyongga Bao [a], Yongjie Zhou [d], Tao Li [b,*], Qiang Lu [a,**]

[a] Department of Ultrasound, West China Hospital of Sichuan University, Chengdu, 610041, China
[b] Department of Anesthesiology, National Clinical Research Center for Geriatrics, West China Hospital of Sichuan University, Chengdu, 610041, China
[c] Laboratory of Ultrasound Medicine, West China Hospital of Sichuan University, Chengdu, 610041, China
[d] Department of Liver Transplantation Center & Laboratory of Liver Transplantation, West China Hospital of Sichuan University, Chengdu, 641400, China
[e] Liver Transplant Center, Transplant Center, West China Hospital, Sichuan University, Chengdu, 610041, China
[f] Laboratory of Hepatic AI Translation, Frontiers Science Center for Disease-Related Molecular Network, West China Hospital, Sichuan University, Chengdu, 610041, China

ARTICLE INFO

Keywords:
Hepatocellular carcinoma
Thermal ablation
H3K18la
NFS1
Oxaliplatin

ABSTRACT

Insufficient microwave ablation (IMWA) is linked to aggressive hepatocellular carcinoma (HCC) progression. An increase in lactate levels after sublethal heat stress (HS) has been confirmed in HCC. However, the role of lactate-related histone lactylation in the progression of HCC caused by sublethal HS remains unclear. Here, we found that the metastatic potential of HCC increased in a lactate-dependent manner after IMWA. Moreover, sublethal HS triggered an increase in H3K18la modification, as validated in a cell-derived xenograft mouse model and human HCC samples. By performing an integrated analysis of proteomic and transcriptomic profiles, we revealed that HCC cells exhibited increased intracellular iron ion homeostasis and developed resistance to platinum-based drugs after exposure to sublethal HS. We subsequently integrated proteomic and transcriptomic data with H3K18la-specific chromatin immunoprecipitation (ChIP) sequencing to identify candidate genes involved in sublethal heat treatment-induced HCC cell metastasis. Mechanically, an increase in H3K18la modification enhanced the transcriptional activity of NFS1 cysteine desulfurase (NFS1), a key player in iron–sulfur cluster biosynthesis, thereby reducing the susceptibility of HCC to ferroptosis after IMWA. Knocking down NFS1 diminished the metastatic potential of sublethally heat-treated HCC cells. Additionally, NFS1 deficiency exhibited a synergistic effect with oxaliplatin, leading to the significant inhibition of the metastatic capability of HCC cells both in vitro and in vivo, regardless of sublethal HS treatment. In conclusion, our study revealed the oncogenic role of histone lactylation in HCC after IMVA. We also bridged histone lactylation with ferroptosis, providing novel therapeutic targets for HCC following microwave ablation, particularly when combined with oxaliplatin-based chemotherapy.

1. Introduction

Hepatocellular carcinoma (HCC) is the sixth most prevalent type of cancer, with its mortality rate ranking third among all causes of death related to tumors [1]. Thermal ablation, exemplified by both microwave ablation and radiofrequency ablation, has been widely applied in clinical practice [2]. Compared with hepatectomy, local thermal ablation is increasingly recognized as a radical treatment method for early HCC because of its minimal invasiveness and comparable treatment outcomes [3]. Nevertheless, postablation recurrence induced by insufficient microwave ablation (IMWA) remains the primary obstacle associated with microwave ablation. The reported median intrahepatic recurrence time is 27.6 months, with 5- and 10-year recurrence rates of 68.8 % and 79.4 %, respectively [4]. Additionally, microwave ablation generates a local temperature field, with a decreasing distribution from the center to the periphery. While a high temperature in the central area induces

* Corresponding author. West China Hospital, Sichuan University No. 37 Wainan Guoxue Road, Chengdu 610041, Sichuan, China.
** Corresponding author. West China Hospital, Sichuan University No. 37 Wainan Guoxue Road, Chengdu 610041, Sichuan, China.
E-mail addresses: scutaoli1981@scu.edu.cn (T. Li), luqiang@scu.edu.cn (Q. Lu).
[1] These authors contributed equally to this work.

https://doi.org/10.1016/j.redox.2025.103553
Received 6 February 2025; Accepted 15 February 2025
Available online 15 February 2025

coagulation necrosis of the local tumor, a sublethal temperature zone emerges at the periphery of the ablation site, hindering complete tumor clearance and resulting in tumor residue. Moreover, a sublethal temperature has the potential to stimulate tumor cell metastasis, thereby fostering the progression of residual tumors [5,6].

Normally differentiated cells rely primarily on oxidative phosphorylation in mitochondria for cellular energy, whereas most tumor cells rely on aerobic glycolysis, a phenomenon known as the Warburg effect [7]. A previous study reported that HCC cells exhibit an increase in glucose uptake and lactate production, i.e., an increase in the Warburg effect, after exposure to sublethal heat stress (HS) [8]. Lactate, as an energy supply, contributes to HCC proliferation and metastasis. Lactate modulation is believed to be a critical regulator of tumor progression [9,10]. However, the role of increased lactate levels in IMWA-induced HCC progression remains poorly understood.

Lactate-derived histone lactylation regulates gene transcription [11]. Lactylation functions as a crucial epigenetic regulator during oncogenesis. For example, elevated H3K18la modification at the YTH N6-methyladenosine RNA-binding protein 2 gene locus has been found to accelerate tumorigenesis in ocular melanoma [12]. Histone lactylation also plays a pivotal role in the pathogenesis of clear cell renal cell carcinoma [13]. Global lactylome profiling of a prospectively collected hepatitis B virus-related HCC cohort indicated that lactylation might contribute to HCC progression [14]. In addition, the inhibition of H3 histone lactylation has been shown to suppress HCC tumorigenicity [15]. Thus, histone lactylation in tumors is very likely to be aberrant, necessitating the exploration of the potential function of histone lactylation in tumorigenesis. The results of the aforementioned studies point toward a potential role for lactylation in HCC progression after IMWA.

Ferroptosis is an iron-dependent form of programmed cell death characterized by glutathione depletion, resulting in a decrease in glutathione peroxidase (GPX4) activity and lipid peroxidation [16]. Accumulating evidence has shown that ferroptosis is associated with HCC proliferation, metastasis and drug resistance. The iron–sulfur cluster biosynthetic enzyme NFS1 cysteine desulfurase (NFS1) is particularly important for maintaining the activity of the iron–sulfur cluster. NFS1 suppression alone does not induce ferroptosis in lung adenocarcinoma, but when NFS1 is combined with the inhibition of cystine transport, iron starvation induced by NFS1 inhibition promotes ferroptosis [17]. Data from 159 hepatitis B virus-related HCC patients indicated that the expression of NFS1 is greater in tumor tissues than in paired adjacent liver tissues [18]. Compared with that in hepatocytes, iron–sulfur cluster biosynthesis is significantly higher in HCC cells [18]. The results of the aforementioned studies suggest the possibility of decreased ferroptotic vulnerability during HCC progression, including sublethal HS-induced metastasis.

Oxaliplatin (OXA) has shown measurable efficacy following surgery and subsequent therapy in HCC patients. However, a substantial number of HCC patients do not respond to OXA because of primary resistance or acquired resistance [19–21]. Protein arginine methyltransferase 3 has been identified as an important regulator of OXA resistance in HCC [22]. In a study related to platinum-based chemotherapy in colorectal cancer, NFS1 was reported to be associated with hyposensitivity to chemotherapy, and NFS1 inhibition combined with OXA triggered PANoptosis, including ferroptosis [23]. However, the precise mechanistic involvement of ferroptosis in determining chemosensitivity in HCC remains inadequately elucidated.

In the present study, we determined that sublethal HS-induced HCC metastasis was lactate dependent. The inhibition of lactate production efficiently suppressed tumor progression. Lactate-dependent H3K18la levels were increased in IMWA models. Using a multiomics approach, we demonstrated that H3K18la promoted the transcription of NFS1, which is essential for the biosynthesis of iron–sulfur clusters. NFS1 knockdown reduced the ability of HCC to metastasize and increased the susceptibility of HCC cells to ferroptosis. Additionally, the combination of NFS1 inhibition with OXA treatment significantly reduced HCC cell migration and invasion. Therefore, our data revealed a novel mechanism by which H3K18la modulates ferroptosis during HCC progression after IMWA and demonstrated that the loss of NFS1 increased the treatment sensitivity of HCC to OXA.

2. Materials and methods

2.1. Clinical patients, tissue microarray, and survival analysis

We studied 323 patients with complete clinical and prognostic information who were diagnosed with hepatocellular carcinoma (HCC) and who underwent hepatectomy at West China Hospital of Sichuan University between March 2015 and December 2019. The tissue microarray (TMA) was prepared from formalin-fixed and paraffin-embedded samples of HCC. Semiquantitative analysis of protein expression after immunohistochemical (IHC) staining was performed as previously described [22,23]. Briefly, the expression levels of HK1 and PFKL in HCC samples were assessed using the H-SCORE, and the patients were subsequently categorized into high- or low-expression groups on the basis of their scores. The overall survival (OS) of patients was defined as the duration from initial hepatectomy to death, while 2-year disease-free survival (DFS) was measured from the time of tumor resection until recurrence or death resulting from HCC.

To investigate the influence of IMWA on HCC progression, we retrospectively studied a cohort of patients with comprehensive clinical data who were diagnosed with HCC in our hospital. Twenty patients who underwent tumor resection due to in situ tumor recurrence after microwave ablation were assigned to the post-IWMA group, and 24 patients who underwent radical resection due to tumor relapse after initial surgical resection (SR) were assigned to the post-SR group.

The study protocol was approved by the Ethics Committee of West China Hospital of Sichuan University, and the study has been registered at the China Clinical Trials Registry (Registration No. ChiCTR2000039018).

2.2. Animals

All the animal experiments were performed after obtaining the approval of the Institutional Animal Care and Use Committee of West China Hospital, Sichuan University, China (Protocol# 2020040A). The experiments were conducted with at 5–6-week-old male nude mice (BALB/c nu/nu), which were provided by Charles River (Beijing, China). All the mice were fed under pathogen-free conditions. All the mice were bred and housed at 22 °C and a relative humidity of 40%–60 % with a 12-h light–dark cycle and had free access to water and food.

2.3. Cell lines

Two human HCC cell lines (Huh7 and MHCC-97H) were used in this study. Huh7 (300156CP, Cel1 line service, Germany) and MHCC-97H (Manassas, American Type Culture Collection, VA, America) cells were maintained in DMEM (GIBCO) supplemented with 10 % (v/v) fetal bovine serum (GIBCO) and cultured at 37 °C in 5 % CO_2.

2.4. Sublethal heat stress cell assay

Cells were incubated in a 37 °C thermostatic incubator for 24 h. The medium was then replaced with pre-warmed 47 °C medium, and the plates were subjected to a 47 °C water bath for 15 min. Following treatment, the medium was replaced with fresh 37 °C medium, and the plates were maintained in the incubator for an additional 24 or 48 h before subsequent assays.

2.5. Cell proliferation assays

HCC cells (8×10^3) were seeded into 96-well plates (Corning)

containing 100 μL of complete medium. Cell proliferation was assessed using CCK-8 assays (Beyotime, C0038) at 1, 2, 3, 4, and 5 days according to the manufacturer's instructions.

2.6. In vitro migration and invasion assays

The migratory or invasive ability of HCC cells was determined using 24-well transewell inserts (Corning, NY, USA). The lower chamber was filled with DMEM containing 10 % FBS as a chemoattractant. Different cells were seeded at a density of 5×10^4 in serum-free medium in the upper chamber and incubated at 37 °C in a humidified incubator containing 5 % CO_2 for 48 h (migration assay) or 72 h (invasion assay). Cells that migrated to the underside of the membrane were stained with crystal violet (C0775), imaged, and quantified using an Olympus IX83 microscope and Nikon C2 imaging system. All experiments were performed in duplicate, and cell numbers from 5 representative images per group were used for statistical analysis.

2.7. Fluorescence imaging of cytoskeletal proteins

F-actin, along with two cytoskeletal proteins, paxillin and vinculin, were simultaneously assayed. MHCC-97H cells were seeded at a density of 4×10^4 cells per well in a confocal dish and treated accordingly. The cells were then washed with PBS, fixed with 4 % paraformaldehyde (Cat. No. BL539A, Biosharp, China), and permeabilized with 0.1 % Triton X-100 (Cat. No. T8200, Solarbio, China) at room temperature. Next, the samples were incubated overnight at 4 °C with a rabbit monoclonal antibody against paxillin (Cat. No. ab32084, Abcam) and a mouse monoclonal antibody against vinculin (ab130007, Abcam). Prior to that, the cells underwent three washes with PBS before being incubated for 60 min with Alexa Fluor 594 donkey anti-mouse IgG (H + L) antibody (Cat.No.34112ES60, Yeasen) and Alexa Fluor 647 donkey anti-rabbit IgG (H + L) antibody (Cat.No34213ES60, Yeasen). Following this step, the cells were stained using Acti-stain™488 Fluorescent Phalloidin (Cat. No.#PHDG1, Cytoskeleton), and DAPI staining was conducted for10 min. The intensity of the cells was tested using confocal lasers canning microscopy (LSM980, ZEISS, Germany).

2.8. Cell line-derived xenograft and lung metastasis model

All surgical procedures were conducted under anesthesia via sodium pentobarbital. A total of 4×10^6 MHCC-97H cells were injected subcutaneously into the right axilla of the mice. When the tumors grew to 250 mm^3 in size, tumor tissue was cut into 2 × 2 mm pieces and implanted into the liver. Four weeks after implantation, insufficient microwave ablation was performed. Tumor tissues were harvested before and 4 h after microwave ablation. Lung metastasis models were established by intravenously injecting 1×10^6 MHCC-97H cells into each mouse through the tail vein. After 6 weeks, the mice were sacrificed. To explore the effect of OXA, the mice were treated with an i.p. injection of PBS or OXA (7.5 mg/kg every 3 days until day 30).

2.9. Western blot

The cells were homogenized in RIPA buffer supplemented with a protease inhibitor cocktail (Roche). The protein supernatant was obtained through centrifugation, and the protein concentrations were determined using a BCA protein assay kit (Bio-Rad). Subsequently, the samples were denatured with loading buffer and stored at −20 °C until further analysis. Protein samples (20–40 μg) were subjected to electrophoresis on SDS−polyacrylamide gels, followed by transfer of the proteins onto PVDF membranes. The membrane strips were then blocked for 1 h at room temperature using a blocking solution containing 5 % BSA in Tris-buffered saline (TBS; 150 mM NaCl, 50 mM Tris Base, pH 7.6) with the addition of 0.1 % Tween 20. Subsequently, the membranes were incubated overnight at 4 °C with primary antibodies. After three washes with TBST, horseradish peroxidase (HRP)-conjugated secondary antibodies (Proteintech #SA00001-1 and #SA00001-2) were applied to the membranes. Signal intensities were visualized using an enhanced chemiluminescence Western blot detection kit (ECM #P10100). Band intensities were quantified using ImageJ software. Primary antibodies were listed in Supplementary Table 3.

2.10. Insufficient microwave ablation

Insufficient microwave ablation was performed using tumor-bearing BALB/c-nude mice with a microwave ablation instrument (Great Wall Microwave ablation instrument, model MTI-5A; ablation needle model XR-A1610 W). The needle electrodes were inserted into the liver tumor along the long axis of the tumor under ultrasound guidance. The insertion distance was approximately 1/2 of the length of the liver tumor, the ablation power was 30 W, and the time was 15–20 s. After ablation, the sizes of the ablated necrotic and residual tumors were evaluated via contrast-enhanced ultrasound, and images were saved for subsequent analysis.

2.11. RNA extraction and RT-qPCR

The cells were homogenized in TRIzol reagent (Life Technologies, Inc.) for RNA extraction. Each sample's total RNA (2 μg) was reverse transcribed into cDNA utilizing a first-strand cDNA synthesis kit (MBI Fermentas, Hanover, Germany). RT-qPCR analysis was conducted employing a one-step SYBR Prime ScriptTM RT-qPCR kit (Perfect RealTime; Takara Bio Inc., Tokyo, Japan), along with an ABI Prism 7000 sequence detection system (Applied Biosystems, Foster City, CA), following the manufacturer's guidelines. The relative mRNA expression levels were determined using the ΔΔCt method and standardized against β-actin levels. The primer sequences utilized for RT-qPCR can be found in Supplementary Table S2.

2.12. Seahorse XF assays

Hydrate the probe plate one day prior to the experiment. On the day of the experiment, immerse the probe plate sensor in XF calibration solution and place it in a 37 °C CO_2-free cell culture incubator for 45–60 min to ensure hydration. Sequentially add Oligomycin (Oligo), FCCP, and Antimycin A/Rotenone (AA/R) to the probe plate for calibration purposes. Once calibrated, insert it into the cell plate to measure cellular oxygen consumption rate (OCR). For extracellular acidification rate (ECAR) measurement: Pre-hydrate the probe plate and place it in a 37 °C CO_2-free cell culture incubator for 45–60 min before conducting the experiment. Sequentially add Glucose, Oligo, and 2-Deoxyglucose (2-DG) to calibrate the probe plate. After calibration, transfer it to the cell plate for ECAR measurement.

2.13. Measurement of lactate levels

Cells were collected and homogenized with lactate assay buffer. The suspension was sonicated at 300 W (3 s on and 7 s off) for 3 min on ice and centrifuged at 12,000×*g* for 10 min at 4 °C. The lactate levels were measured using a Lactate Colorimetric Assay Kit (BioVision K607-100) according to the manufacturer's instructions.

2.14. Lentivirus-mediated knockdown of gene expression

For lentivirus generation, 1×10^7 293T cells were seeded in 10-cm dishes in DMEM supplemented with 10 % FBS the day before transfection. The cells were transfected with 4 μg of pLKO shRNA, pLKO shLDHA, or pLKO shNFS1 combined with 3 μg of psPAX2 and 1 μg of pMD2.G in 10 mL of DMEM (GIBCO) containing 16 μL of Lipofectamine 2000 (Thermo Fisher Scientific, 11668027). Six hours later, the medium was changed to DMEM supplemented with 10 % FBS. After 48 h, the

supernatant was recovered, filtered through 0.45 μm filters and used to infect HCC cell lines. Stable cell lines were obtained via puromycin selection for 1 week. The short hairpin sequences used for gene silencing are shown in Supplementary Table S3.

2.15. Hematoxylin and eosin staining and immunohistochemistry

Tissues were fixed by immersion in 4 % paraformaldehyde for 6 h. Then, the samples were immersed in 10 % sucrose at 4 °C overnight, followed by 30 % sucrose at 4 °C overnight. Tissues (8 μm) were sectioned with a freezing microtome (CM1850; Leica, Buffalo Grove, IL, USA). For H&E staining, the sections were stained with hematoxylin for 10 min and eosin for 30 s, washed in 0.5 % hydrochloric acid alcohol, dehydrated and mounted. For immunohistochemistry, all the sections were deparaffinized in xylene and rehydrated through a series of alcohol washes. After rehydration, the sections were microwaved in citric acid buffer (10 mM, pH 6.0) for antigen retrieval, and endogenous peroxidase activity was blocked with 3 % H_2O_2 at room temperature for 10 min. The sections were then blocked with 5 % goat serum for 1 h at room temperature and incubated overnight at 4 °C with primary antibodies. The following primary antibodies were used: anti-HK1 (Cell Signaling, #2024), anti-PFKL (Proteintech, 68385-1-1g), anti-H3K18la (PTM-Bio, PTM-1406RM) and anti-NFS1 (Proteintech, 15370-1-AP). Images were acquired with an Olympus IX83 and Nikon C2.

2.16. Transcriptome sequencing

Total RNA was extracted using TRIzol (Invitrogen, CA, USA) according to the manufacturer's instructions. RNA purity and quantity were assessed using a NanoDrop 2000 spectrophotometer (Thermo Scientific, USA). RNA integrity was evaluated using an Agilent 2100 Bioanalyzer (Agilent Technologies, Santa Clara, CA, USA). Libraries were subsequently prepared using a VAHTS Universal V6 RNA-seq Library Prep Kit following the manufacturer's instructions. Transcriptome sequencing and analysis were performed by OE Biotech Co., Ltd. (Shanghai, China). Significantly differentially expressed genes (DEGs) were identified as those with P values < 0.05 and a fold change >2 or < 0.5.

2.17. Protein extraction, digestion, LC–MS, protein identification and quantification

One hundred milligrams of frozen sample was rapidly ground into a fine and uniform powder in liquid nitrogen, followed by homogenization in 1 mL of phenol extraction buffer. After shaking several times, the mixture was kept at 4 °C for 30 min. The upper phenolic phase was separated from the aqueous phase by centrifugation (7100×g) at 4 °C for 10 min. After an overnight incubation at −20 °C, the mixture was centrifuged (12,000×g) at 4 °C for 10 min to pellet the precipitated protein. The protein concentration was quantified using a bicinchoninic acid assay. In the protein digestion step, protein samples were diluted to the same concentration and volume. DTT (25 mM) was added to the protein mixture, followed by incubation at 55 °C for 30–60 min. After cooling on ice to room temperature, the corresponding volume of iodoacetamide (final concentration of approximately 10 mM) was added, and the mixture was incubated in the dark at room temperature for 15–30 min. Six times the volume of precooled acetone was added to precipitate the protein, which was subsequently stored at −20 °C for more than 4 h or overnight. After precipitation, the precipitate was collected by centrifugation at 8000×g for 10 min at 4 °C, followed by a standing time of 2–3 min to allow the acetone to evaporate. To redissolve the protein precipitate, 100 μL of NH4HCO3 solution (50 mM) was added. Depending on the amount of protein, an appropriate volume of enzymolysis diluent (protein: enzyme = 50:1 w/w; e.g., for every 100 μg of protein, 2 μg of enzyme) was added, and then, the solutions were digested at 37 °C for either 12 h or overnight. The enzymatic reaction was stopped by adjusting the pH to 3 with phosphoric acid. The samples were desalted using SOLA™ SPE. After vacuum drying, the samples were resuspended, and iRT peptides (at a ratio of 1:10) were added. Proteomic data analysis was conducted by Shanghai OE Biotech Co., Ltd. (Shanghai, China). All analyses were performed using a Tims TOF Pro mass spectrometer (Thermo, Bruker) equipped with an Easyspray source (Thermo, USA). A total of 8070 proteins expressed in the proteome of the human HCC cell line MHCC-97H were identified in this study. A fold change (>2.0 or <1) and a P value < 0.05 were the thresholds used to identify DEPs.

2.18. Chromatin immunoprecipitation sequencing (ChIP-seq)

ChIP-seq assays were performed according to the manufacturer's protocol (Cell Signaling Technology, #9005). In brief, MHCC-97H cells were crosslinked with formaldehyde, after which glycine was added to quench the unreacted formaldehyde. The cells from each dish were scraped into 1 × PBS and centrifuged at 800×g for 5 min. The pellets were subsequently resuspended in nuclear lysis buffer. After the resulting suspension was sonicated, the lysate was incubated with an anti-H3K18la antibody (PTM-Bio, PTM-1427RM) and protein G magnetic beads overnight at 4 °C and then reverse crosslinked. ChIP-seq analysis was performed by Wuhan IGENEBOOK Biotechnology Co., Ltd. (Wuhan, China). Genes with a peak within 3 kb of the transcription start site were considered target genes and were annotated via the Kyoto Encyclopedia of Genes and Genomes. Visualization of the peak distribution along the genomic regions of NFS1 was performed with Integrative Genomics Viewer.

2.19. Cell viability and cytotoxicity assay

Cell viability and cytotoxicity were evaluated with a Calcein/PI Cell Viability/Cytotoxicity Assay Kit (Cat. No. C2015 M, Beyotime). Cells were seeded at 4×10^4 per well in a 12-well plate. After the indicated treatment, the cells were stained with 500 μL of working solution for 30 min according to the manufacturer's instructions. Live and dead cells were stained with calcein-AM (green) and PI (red) solutions, respectively. The cells were analyzed using a fluorescence microscope (IX83, Olympus, Japan) and a flow cytometer (CytoFLEX, Beckman, USA) at excitation/emission wavelengths of 494 nm/517 nm and 540 nm/590 nm, respectively.

2.20. Intracellular Fe^{2+} accumulation

Intracellular Fe^{2+} accumulation was assessed using a FerroOrange live cell probe (Cat. No. MX4559-24UG, MKBio); FerroOrange was dissolved in DMSO and diluted according to the manufacturer's instructions. After the indicated treatment, HCC cells were seeded at a density of 4×10^4 cells per well in a confocal dish and stained with 250 μL of FerroOrange working solution for 30 min. Nuclei were subsequently labeled with Hoechst (Cat. No. C1026, Beyotime). The intracellular fluorescence intensity of FerroOrange (Ex/Em = 540/590 nm) was observed using a confocal laser scanning microscope (LSM980, Zeiss, Germany).

2.21. Intracellular ATP release

Intracellular ATP release was evaluated with a commercially available ATP assay kit (Cat. No. S0027, Beyotime). Briefly, HCC cells were seeded at 4×10^4 cells per well in a 12-well plate and treated accordingly. After cell lysis, the supernatant was collected by centrifugation, and ATP detection working solution was added to the supernatant. The ATP concentration was measured using a fluorescence microplate reader and quantified using a standard curve.

2.22. Malondialdehyde measurement and lipid ROS assay

Malondialdehyde levels were measured using a thiobarbituric acid reactive substances (TBARS) assay kit (Cat. No. 10009055, Cayman Chemical) according to the product instructions. For lipid ROS assays, cells were seeded at 3×10^4 per well in a 48-well plate. After the indicated treatment, the cells were incubated with 5 μM BODIPY™ 581/591C11 probe (D3861, Thermo Fisher Scientific) in the dark at 37 °C for 1 h. Images were acquired with an Olympus IX83 microscope and Nikon C2.

2.23. Mitochondrial membrane potential (ΔΨm) assay

ΔΨm was evaluated using a JC-10 assay kit (Cat. No. 40752ES60, Yeasen) according to the product instructions. shNC-transfected or shNfs1-transfected HCC cells were seeded at a density of 6×10^5 cells/well in 6-well plates. After the indicated treatment, the cells were incubated with 500 μL of working solution for 20 min. J-monomers and J-aggregates were detected via confocal laser scanning microscopy (LSM980, Zeiss, Germany) and flow cytometry (CytoFLEX, Bechman) at 490/525 and 540/590 nm (excitation/emission), respectively.

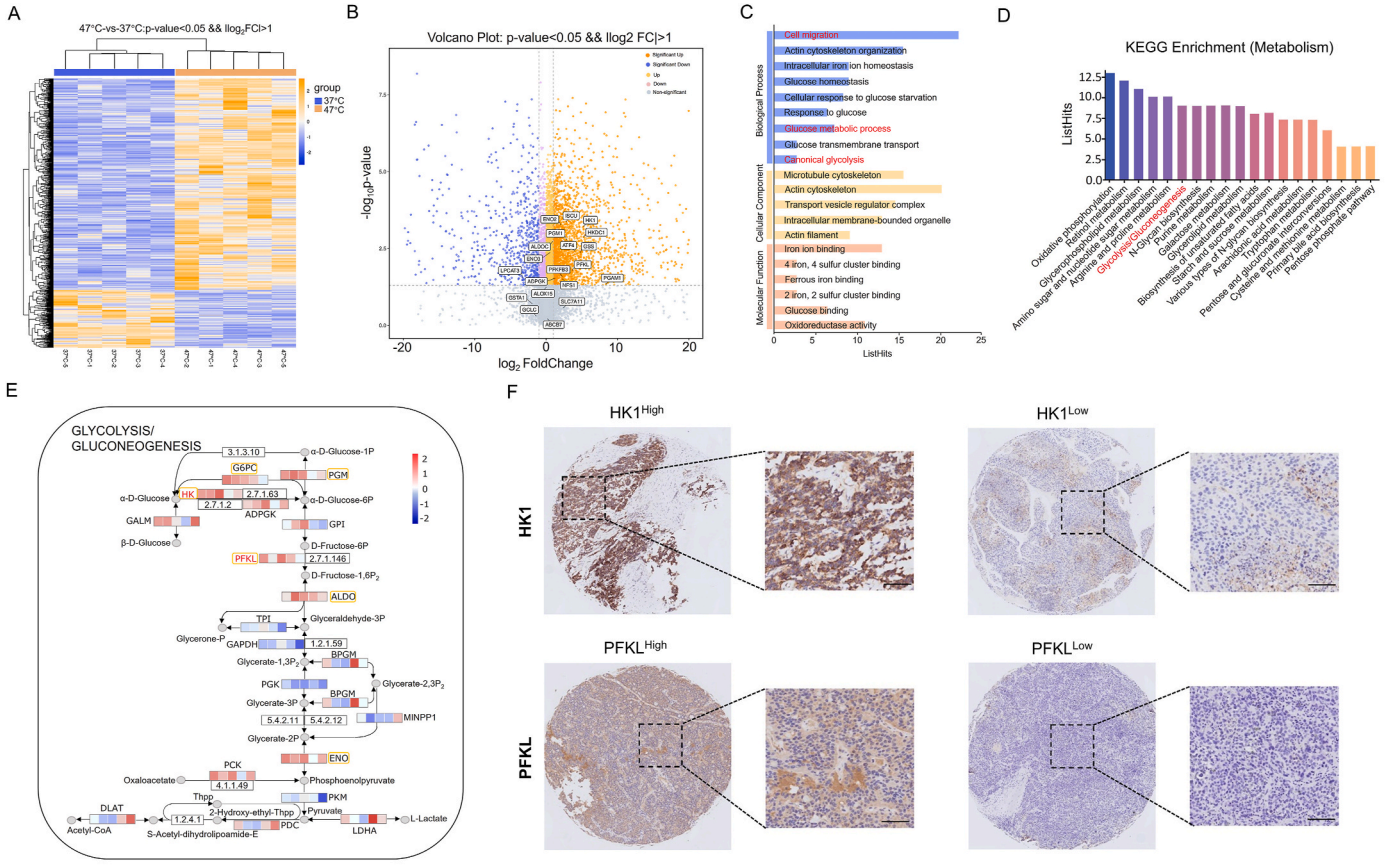

Variables	HK1 Low (n=74)	HK1 High (n=74)	HK1 P value	PFKL Low (n=88)	PFKL High (n=87)	PFKL P value
Sex (male)	60 (81%)	55 (74.3%)	0.3	64 (72.7%)	65 (74.7%)	0.6
Age (yr)	51.2±11.5	54.8±12	0.7	53±11.3	51±12.6	0.3
Cirrhosis (yes)	43 (58.1%)	38 (51.4%)	0.4	42 (47.7%)	51 (58.6%)	0.14
Tumor size (cm)	5.4±3	6.7±3.9	0.02	5.5±2.4	6.5±3.3	0.01
AFP (>20ng/mL)	47 (68.1%)	41 (56.9%)	0.17	57 (64.7%)	51 (58.6%)	0.4
CEA (>5ng/mL)	8 (12.3%)	13 (18.6%)	0.3	5 (8.5%)	6 (10%)	0.8
MVI (yes)	25 (36.2%)	34 (47.9%)	0.005	32 (36.4%)	42 (48.3%)	0.1
Differentiation (well/moderate-poorly)	26/48	36/38	0.04	48/40	39/48	0.2
BCLC staging (A/B/C)	52/18/4	49/22/3	0.7	62/23/5	58/24/7	0.7

Fig. 1. Sublethal heat stress (HS) increases glycolysis in HCC. (A) Heatmap showing the differentially expressed genes (DEGs) after sublethal HS treatment. (B) Volcano plot of transcriptomic analysis results for control vs. HS HCC cells. Significantly increased and decreased protein levels are indicated by orange and blue dots, respectively (n = 5 per group). (C) Gene Ontology (GO) enrichment analysis showing upregulated GO terms, with red highlighting the key GO terms of interest. (D) Kyoto Encyclopedia of Genes and Genomes (KEGG) analysis showing the top 20 metabolic pathways based on transcriptome sequencing data. (E) Heatmap of KEGG pathways showing the DEGs in the glycolysis/gluconeogenesis pathway between control and HS-treated HCC cells. (F) Representative images of HK1 and PFKL immunohistochemistry (IHC) staining of hepatocellular carcinoma (HCC) tissue microarrays. Scale bar, 50 μm. (G) The associations between the expression levels of HK1 and PFKL and the presence of microvascular invasion (MVI) and tumor size in patients with HCC. (H) Correlation analysis between HK1 and PFKL expression and critical clinicopathological characteristics of patients with HCC. (I, J) Correlations between HK1 and PFKL expression and the 2-year disease-free survival (DFS) and overall survival (OS) of patients with HCC. See Supplementary Fig. 1 for supplementary data.

2.24. Transmission electron microscopy

Cells were fixed in 2.5 % glutaraldehyde for 24 h, followed by incubation with 1 % osmium tetroxide for 1 h. After dehydration in ethanol, the cells were embedded in Epon 812. Ultrathin sections (50 nm) were stained with uranyl acetate for 15 min, followed by lead citrate for 1 min. Images were captured under a transmission electron microscope (JEM-1400PLUS, JEOL, Japan).

2.25. Reagents

The following reagents were used: 2-deoxy-D-glucose (MCE, HY-13966), sodium dichloroacetate (MCE, HY-Y0445A), sodium oxamate (MCE, HY-W013032A), lactate (MCE, HY-B2227), erastin (MCE, HY-15763) and oxaliplatin (Sichuan Huiyu Pharmaceutical Co., Ltd.; 2312302412).

2.26. Data analysis

Statistical analysis was performed using GraphPad Prism v.8.0.1 (GraphPad, La Jolla, CA). All the data are presented as standard deviation (SD). The Shapiro–Wilk normality test was performed to determine the data distribution. Statistical significance was determined with the unpaired Student's *t*-test (two-tailed) for comparisons between two groups or by one-way ANOVA with Tukey's post hoc test for multiple comparisons. The time course data of the behavioral tests were analyzed using two-way analysis of variance (ANOVA) with repeated measures followed by Bonferroni post hoc correction. Statistical significance is indicated by $*p < 0.05$, $**p < 0.01$, and $***p < 0.001$.

3. Results

3.1. Sublethal HS increases glycolysis in HCC

To determine whether aberrant glycolysis is involved in the progression of HCC induced by sublethal HS, we conducted transcriptome sequencing analysis on an established sublethal HS cell model [8,24]. A visualization of the mRNA expression profile of DEGs between the 37 °C (physiological temperature) and 47 °C (HS) water bath treatments is shown in Fig. 1A. Compared with 37 °C, sublethal HS induced the upregulation of the expression of glycolysis-related genes, including HK1, PFKL, PGM1, HKDC1, ENO2, PGAM1, and PFKFB3 (Fig. 1B). Among the top enriched Gene Ontology (GO) terms, cell migration was the most significantly enriched biological process, while glucose metabolism activity was also significantly enhanced (Fig. 1C). Thereafter, we performed Kyoto Encyclopedia of Genes and Genomes (KEGG) pathway analysis, primarily focusing on metabolic pathways (Fig. 1D). Notably, among the top 20 enriched pathways related to glucose metabolism, oxidative phosphorylation ranked highest, followed by glycolysis/gluconeogenesis. Subsequently, we searched the GEO database of the National Center of Biotechnology Information. The original mRNA expression profiles from tumors and adjacent nontumorous samples in the GSE57957 [25] and GSE76427 [26] datasets were used for subsequent analyses. To investigate the role of glycolysis in HCC, we reviewed three glycolysis gene sets (https://maayanlab.cloud/Harmonizome/gene_set/glycolysis/GeneRIF+Biological+Term+Annotations; https://www.gsea-msigdb.org/gsea/msigdb/human/geneset/HALLMARK_GLYCOLYSIS.html; and https://www.gsea-msigdb.org/gsea/msigdb/cards/KEGG_GLYCOLYSIS_GLUCONEOGENESIS) and identified 141 and 156 overlapping glycolytic genes in the GSE57957 and GSE76427 datasets, respectively (Supplementary Fig. 1A). Furthermore, the expression of glycolic genes such as GAPDH, ENO1, TPI1, and ALDOA was upregulated in HCC tissues (Supplementary Figs. 1B and C). KEGG mapping revealed a series of upregulated genes in the glycolysis pathway (Supplementary Figs. 1D and E). Taken together, these results highlight the critical role of glycolysis in the carcinogenesis of HCC and suggest that it may mediate HCC progression under sublethal HS.

To illustrate the metabolic reprogramming of HCC under sublethal HS in greater detail, we generated a heatmap of KEGG pathways to visualize individual gene expression changes in the glycolysis/gluconeogenesis pathway in sublethal heat-treated HCC cells. Notably, the expression of the rate-limiting enzymes HK1 and PFKL was upregulated in heat-treated HCC cells, an effect that was validated by quantitative reverse transcription polymerase chain reaction (RT–qPCR) (Fig. 1E and Supplementary Fig. 1F). It has been reported that increased HK1 and PFKL expression can accelerate and activate the glycolysis pathway in HCC [27]. To investigate the role of HK1 and PFKL in HCC progression, we assessed their prognostic value using clinical HCC samples from our hospital. Using IHC staining, patients were categorized into groups on the basis of protein expression levels and H-scores: high HK1 expression ($HK1^{High}$) and low HK1 expression ($HK1^{Low}$) groups and high PFKL expression ($PFKL^{High}$) and low PFKL expression ($PFKL^{Low}$) groups (Fig. 1F). Microvascular invasion (MVI) is one of the core risk factors influencing survival outcomes and intrahepatic metastasis after surgery in patients with HCC [28]. In our cohort, $HK1^{High}$ samples presented a greater proportion of MVI than did $HK1^{Low}$ samples. However, the expression of PFKL did not differ between these two groups. The expression levels of HK1 and PFKL were positively correlated with tumor size (Fig. 1G). The correlations between HK1 and PFKL expression and key clinicopathological characteristics in patients with HCC are summarized in Fig. 1H and Supplementary Fig. 1G. There was no significant difference in overall survival (OS) between the $HK1^{High}$ and $HK1^{Low}$ groups. However, patients with $HK1^{high}$ HCC had significantly shorter 2-year disease-free survival (DFS) than patients with $HK1^{low}$ HCC did (Fig. 1I). In addition, $HK1^{High}$ HCC patients had shorter OS and 2-year DFS than did $PFKL^{Low}$ patients (Fig. 1J).

3.2. Sublethal HS promotes HCC cell metastasis in a lactate-dependent manner

To explore the influence of sublethal HS on HCC cells, MHCC-97H and Huh7 cells were exposed to 47 °C for 15 min. A CCK-8 assay revealed that sublethal HS suppressed the viability and proliferative capability of HCC cells (Supplementary Fig. 2A), a result that was consistent with the findings of a previous study [29]. Furthermore, we performed transwell assays at 48 h after sublethal HS treatment and detected increased migration and invasion capacities in HCC cells (Fig. 2A and Supplementary Fig. 1B). To validate the oncogenic function under sublethal HS conditions in vivo, we used a tail vein injection nude mouse model (Fig. 2B). Mice were sacrificed after 4 weeks, after which the lungs were removed. Consecutive sections were taken from every lung tissue block and stained with hematoxylin and eosin (H&E) to evaluate lung metastasis. We observed a greater number of metastatic lesions in the HS group (Fig. 2C and Supplementary Fig. 2C). We subsequently analyzed the influence of sublethal HS on the expression of epithelial–mesenchymal transition (EMT) markers by immunoblotting. Sublethal HS treatment increased the expression of N-cadherin and vimentin and decreased the expression of E-cadherin in HCC cells (Fig. 2D). Furthermore, immunofluorescence (IF) analysis revealed greater F-actin, paxillin, and vinculin expression in MHCC-97H cells treated at 47 °C than in those treated at 37 °C, indicating enhanced cellular motility and migration potential (Supplementary Fig. 2D). Previously, on the basis of GO analysis, we observed the significant enrichment of biological processes related to actin cytoskeleton organization in sublethal-HS HCC cells, accompanied by the enrichment of cellular components associated with microtubules and the actin cytoskeleton. Taken together, these results indicate that HS promotes the metastatic capability of HCC cells.

The Warburg effect, characterized by increased glycolysis and elevated lactate levels, is a defining hallmark of HCC [9]. Sublethal HS has been reported to trigger an enhanced Warburg effect in HCC cells [30], and we hypothesized that the increased metastatic potential is

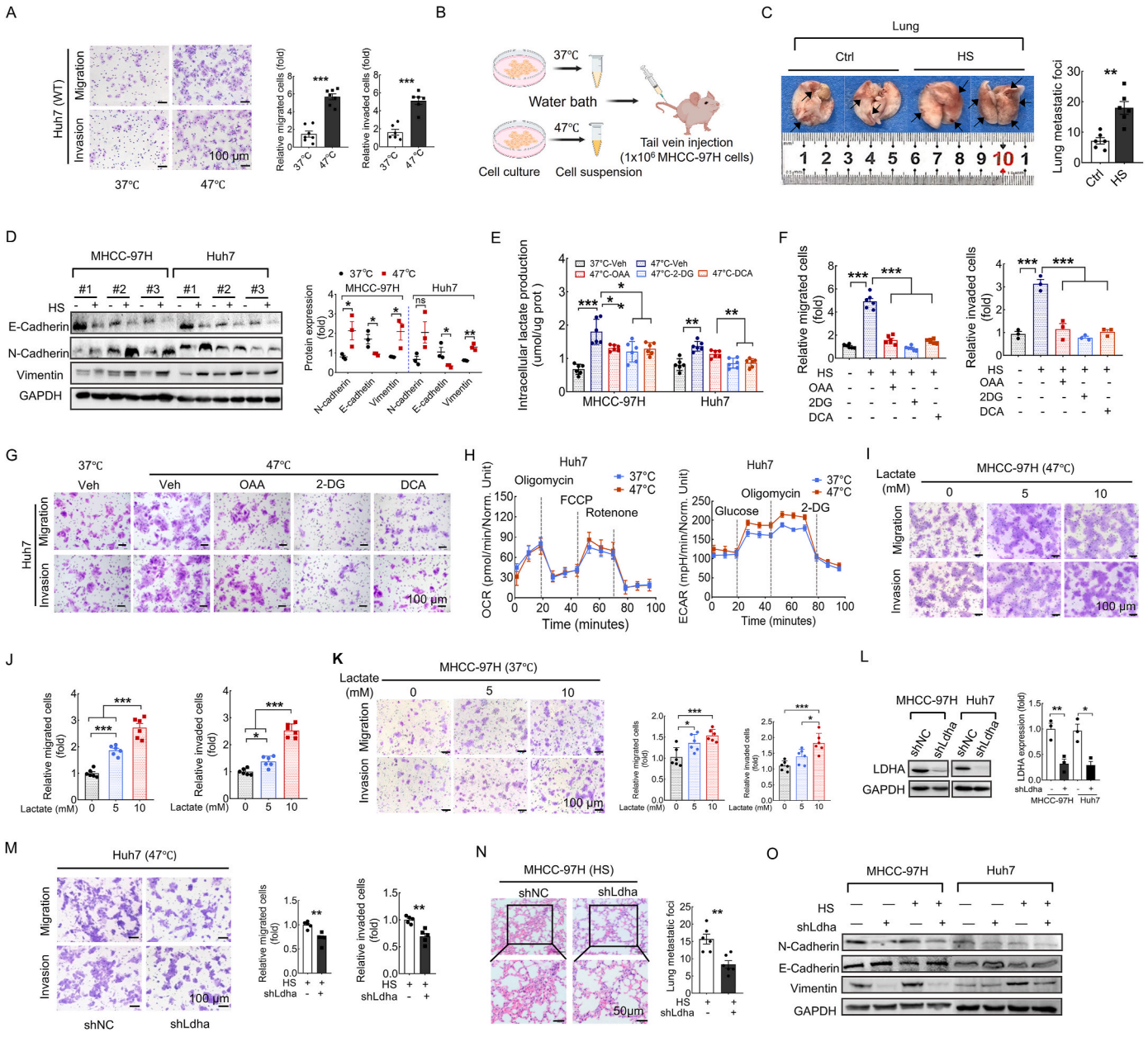

Fig. 2. Sublethal HS promotes HCC cell metastasis in a lactate-dependent manner. (A) Transwell assay showing the migrative and invasive abilities of Huh7 cells at 48 h after exposure to 47 °C or control conditions. Scale bar, 100 μm. (B) A schematic representation of the experimental protocol. After being subjected to a 15-min treatment in a water bath at either 37 °C or 47 °C, MHCC-97H cells were subsequently incubated under normal conditions. The cells were harvested at 48 h for the establishment of an animal model via tail vein injection. (C) Representative macroscopic images and quantitative analysis of lung metastasis four weeks after the intravenous injection of HS or control MHCC-97H cells. (D) Immunoblot analysis and quantification of markers associated with epithelial–mesenchymal transition (EMT) in MHCC-97H and Huh7 cells treated at 37 °C and 47 °C water bath. (E) Intracellular lactate levels in MHCC-97H and Huh7 cells treated with vehicle at 37 °C or with vehicle, OAA, 2-DG or DCA at 47 °C. (F, G) Representative images (G) and quantitative analysis (F) of the migration and invasion of Huh7 cells treated with vehicle at 37 °C or with vehicle, OAA, 2-DG or DCA at 47 °C. Scale bar, 100 μm. (H) Seahorse assay results for the extracellular acidification rate (ECAR) and oxygen consumption rate (OCR) in HS or control Huh7 cells. (I–K) Representative images and quantitative analysis of the migration and invasion of MHCC-97H cells treated with 0, 5, or 10 mM lactate at either 47 °C (I, J) or 37 °C (K). Scale bar, 100 μm. (L) Western blot analysis of LDHA in HCC cells transfected with shNC or shLdha and quantification of LDHA protein levels. (M) Transwell assay demonstrating the migration and invasion abilities of Huh7 cells transfected with shNC or shLdha and treated at 47 °C. Scale bar, 100 μm. (N) Representative H&E staining images and quantification of lung metastases four weeks after the tail vein injection of MHCC-97H cells transfected with shNC or shLdha following exposure to sublethal HS. Scale bar, 50 μm. (O) Immunoblot analysis of EMT-related marker expression in shNC- and shLdha-transfected HCC cells, with or without sublethal HS. See Supplementary Fig. 2 for supplementary data.

driven by lactate. Twenty-four hours after 47 °C or 37 °C water bath treatment, intracellular lactate was measured in MHCC-97H and Huh7 cells. We observed a substantial increase in lactate levels in sublethally heat-treated HCC cells. Conversely, when treated with glycolysis inhibitors—2-deoxy-D-glucose (2-DG; 10 mM), sodium dichloroacetate (DCA; 5 mM), and sodium oxamate (OAA; 5 mM)—lactate production significantly decreased (Fig. 2E). To assess the effect of lactate levels on HCC cell metastasis, we reduced the global intracellular lactate concentration by treating HCC cells with OAA, 2-DG and DCA for 24 h. The inhibition of lactate production reversed the enhanced migration and invasion abilities observed in heat-treated cells (Fig. 2F, G and Supplementary Figs. 2E and F). We subsequently tested the glycolytic and

oxidative phosphorylation activities of Huh7 cells treated at 37 °C and 47 °C via a Seahorse XF24 analyzer over a period of 100 min. Sublethal HS increased the glycolysis level in Huh7 cells, as evidenced by the elevated glycolysis and glycolytic capacity in the extracellular acidification rate (ECAR); the change in the oxygen consumption rate (OCR) was not significant (Fig. 2H). To evaluate the role of lactate in HCC cell metastasis, we treated HCC cells with various concentrations of lactate (0, 5 or 10 mM) for 48 h to investigate its direct effects on the cells. Interestingly, the migration and invasion abilities of MHCC-97H and Huh7 cells, with or without sublethal HS, were enhanced by lactate in a dose-dependent manner (Fig. 2I–K and Supplementary Figs. 2G and H). Lactate dehydrogenase A (LDHA) is the key enzyme that catalyzes the conversion of pyruvate to lactate in the final step of glycolysis. Therefore, we silenced LDHA using hairpin RNA (shLdha and a nontarget shRNA [shNC] as a control) in MHCC-97H and Huh7 cells (Fig. 2L). We found that silencing LDHA decreased the metastatic activity of HCC cells, as the migrative and invasive capabilities of heat-treated HCC cells in the shLdha group were significantly diminished (Fig. 2M and Supplementary Fig. 2I). Similarly, LDHA knockdown significantly suppressed the metastatic potential of HS HCC cells in vivo, as evidenced by lung colonization in the tail-vein injection mouse model (Fig. 2N). Furthermore, the expression of N-cadherin and vimentin, which are markers associated with EMT, was increased in HCC cells regardless of sublethal HS treatment. However, the expression level of E-cadherin was relatively low (Fig. 2O). In brief, these results suggest that sublethal HS promotes HCC cell metastasis in a lactate-dependent

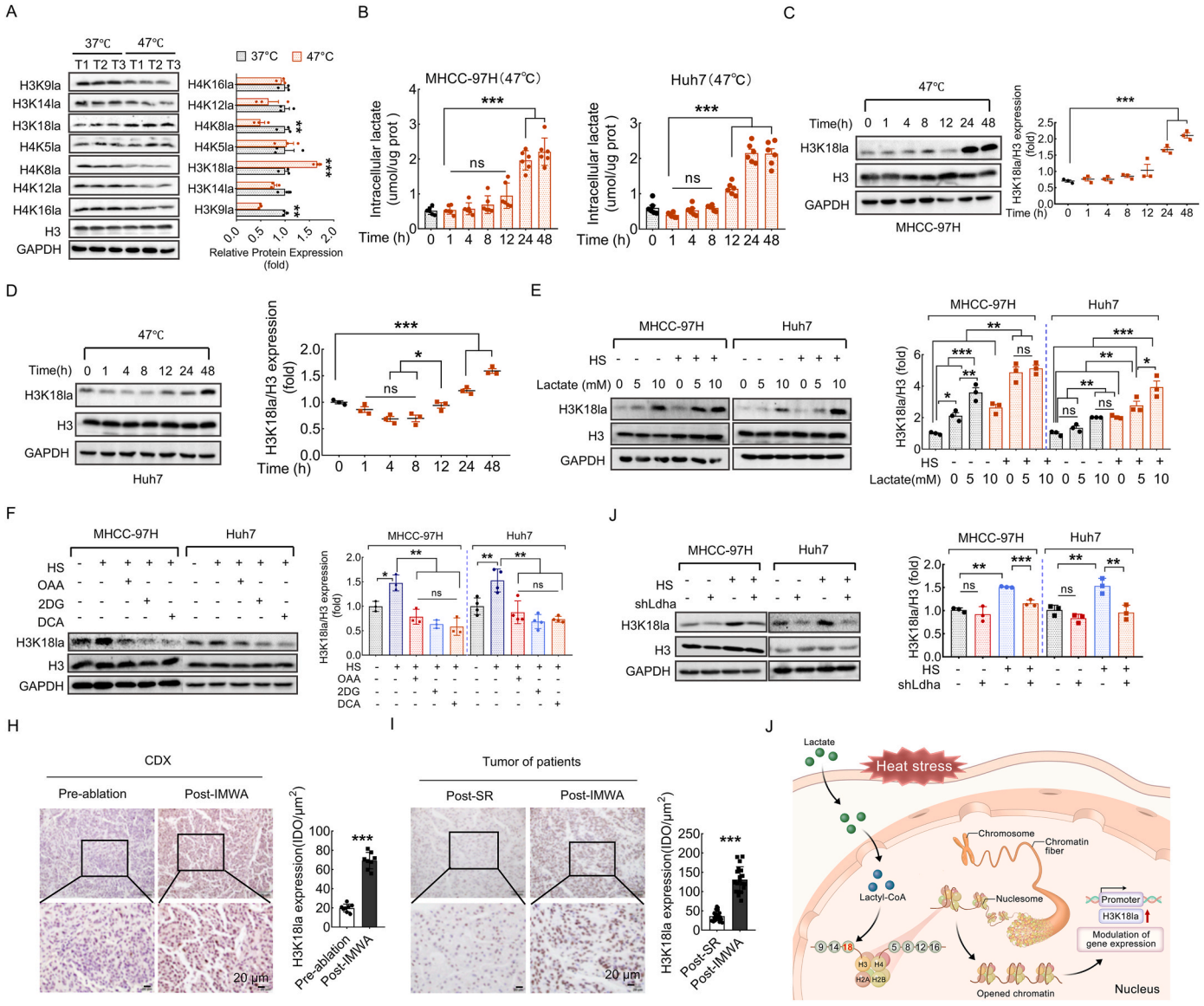

Fig. 3. Sublethal HS promotes H3K18la expression in HCC. (A) Immunoblots showing histone Kla levels at H3K9la, H3K14la, H3K18la, H4K5la, H4K8la, H4K12la, and H4K16la and semiquantitative analysis with ImageJ software. (B) Intracellular levels of lactate in MHCC-97H and Huh7 cells at different time points after sublethal HS. (C, D) Representative Western blot images and quantification of H3K18la in MHCC-97H (C) and Huh7 (D) cells at different time points after sublethal HS. (E) Immunoblot and quantification of H3K18la in HCC cells incubated with 0, 5, or 10 mM lactate after being subjected to either a 47 °C or 37 °C water bath. (F) Representative immunoblot images and quantification of H3K18la in MHCC-97H and Huh7 cells treated with vehicle at 37 °C or with vehicle, OAA, 2-DG or DCA at 47 °C. (J) Immunoblots showing the expression of H3K18la in shNC- and shLdha-transfected HCC cells, with or without sublethal HS. (H) HC staining of H3K18la in cell-derived xenograft (CDX) sections from model mice before and after insufficient microwave ablation (IMWA). Scale bar, 20 μm. (I) IHC staining showing the expression of H3K18la in recurrent HCC samples from patients with HCC following surgical resection (SR) or IMWA. Scale bar, 20 μm. (J) Summary schematic diagram showing the hypothetical role of sublethal HS in increasing intracellular lactate levels, thereby facilitating the enrichment of H3K18la in target gene promoter regions and driving target gene expression.

manner.

3.3. Sublethal HS promotes H3K18la expression in HCC cells

Lactate can modulate epigenetic modifications through histone lactylation and promote the progression of HCC [11]. To investigate the impact of sublethal HS on lactylation, we assessed lactylation at various histone sites in HCC cells. Immunoblotting revealed that among seven histone lactylation sites (H3K9la, H3K14la, H3K18la, H4K5la, H4K8la, H4K12la, and H4K16la), the level of lactylation of histone 3 on lysine residue 18 (H3K18la) was most significantly increased in HCC cells exposed to sublethal HS (Fig. 3A). To study the effects of sublethal HS on the levels of lactate and H3K18la, MHCC-97H and Huh7 cells were harvested at different time points (0, 1, 4, 8, 12, 24 and 48 h) after treatment at 47 °C. Interestingly, the levels of lactate, as well as histone 3 lysine residue 18 (H3K18) lactylation exhibited a significant increase

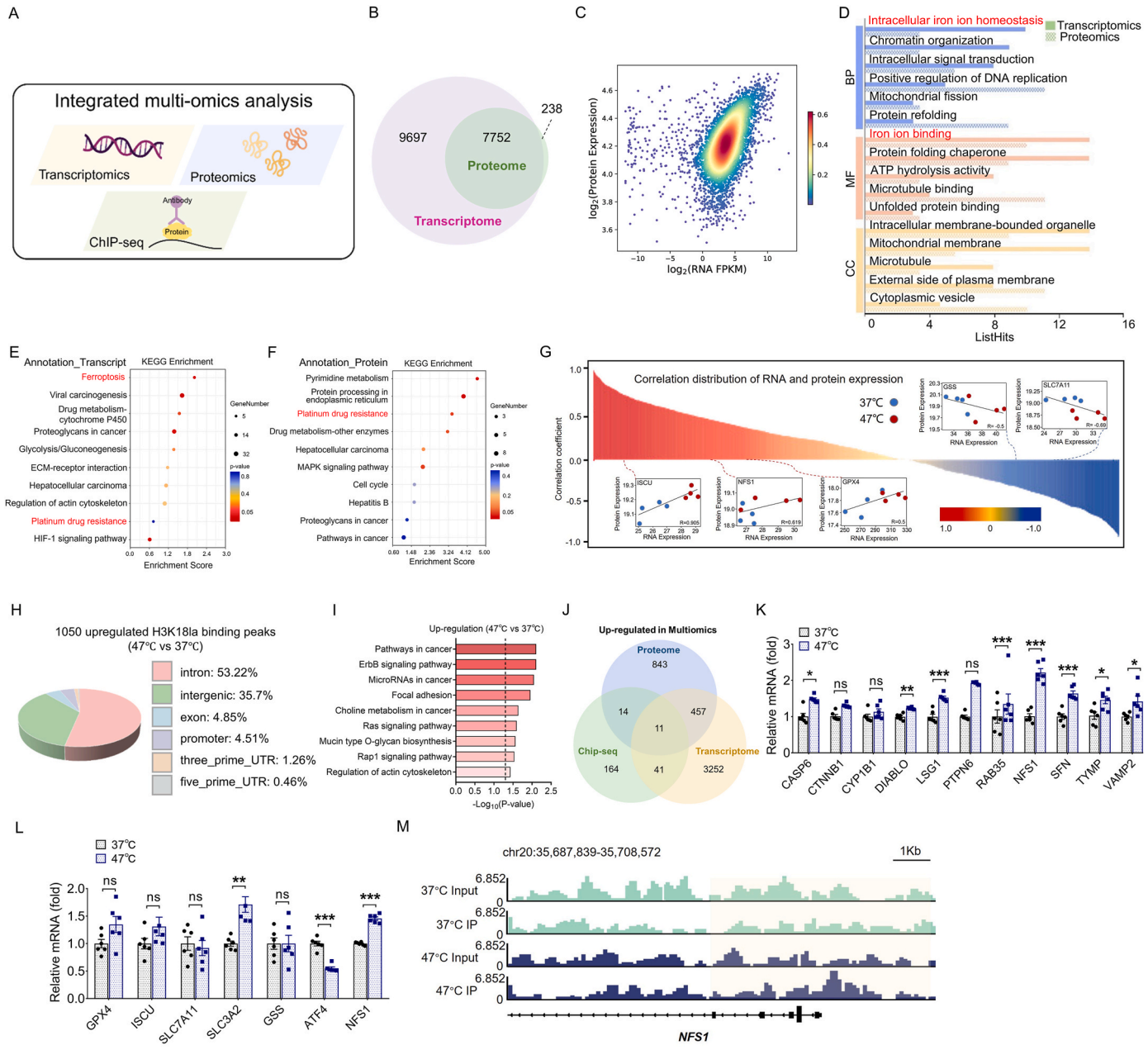

Fig. 4. H3K18a drives NFS1 expression upregulation, suppressing ferroptosis in heat-treated HCC cells. (A) Simplified schematic diagram of the integrated multiomics analyses. (B) Venn diagram of the number of expressed genes identified via transcriptomics and proteomics. (C) A density scatter plot of protein expression intensities versus RNA fragments per kilobase per million (FPKM) values. The color code indicates the density of points. (D) GO annotation results for the integrated transcriptomic and proteomic analysis for sublethal HS vs. control HCC cells. Red indicates the focused GO annotations. (E, F) Bubble chart showing the KEGG results for transcriptomics (E) and proteomics (F). Red represents the pathways of interest. (G) Correlation distribution of the transcriptome–protein pairs in sublethal HS vs. control HCC cells. The red and blue dots indicate the sublethal HS and control treatments, respectively. (H) Distribution of enhanced H3K18la-binding peaks in genomic regions. (B) KEGG and genome analyses of the enhanced H3K18la binding peaks at the promoters of target genes. The dotted line indicates $P < 0.05$. (J) Venn diagram showing the genes that were upregulated and overlapped among the transcriptomic, proteomic, and ChIP-seq analyses. (K) RT–qPCR results for the expression of the eleven overlapping genes based on the omics data after sublethal HS treatment. (L) mRNA expression of representative ferroptosis markers. (M) Integrated genome viewer (IGV) analysis of ChIP-seq signals at NFS1 gene loci. The light-yellow rectangle indicates the peak region of the promoter. See Supplementary Fig. 3 for supplementary data.

in HCC cells after sublethal HS for a duration of 24 h (Fig. 3B–D). To assess the influence of lactate on H3K18la expression, we treated HCC cells with various concentrations of lactate (0, 5, or 10 mM). The expression of H3K18la was upregulated in HCC cells, regardless of HS treatment. Moreover, we observed that heat-treated HCC cells presented higher levels of H3K18la expression than did control HCC cells when the same lactate concentration was administered (Fig. 3E). Moreover, the inhibition of intracellular lactate production by OAA, 2-DG and DCA counteracted the ability of sublethal HS to increase H3K18la expression in heat-treated HCC cells (Fig. 3F). To confirm the link between the intracellular lactate level and H3K18la expression, we assessed the H3K18la level in LDHA-silenced HCC cells. Western blot analysis revealed that inhibiting lactate production via shLdha significantly reversed the upregulation of H3K18la expression induced by sublethal HS. Furthermore, upregulated H3K18la expression was validated in a cell-derived xenograft (CDX) mouse model by IHC (Fig. 3H). To validate the functional role of IMWA in HCC, we retrospectively studied a cohort of patients with HCC at our hospital. Twenty patients who underwent tumor resection due to in situ tumor recurrence after microwave ablation were assigned to the post-IWMA group, and 24 patients who experienced tumor relapse after initial surgical resection were assigned to the post-SR group. IHC staining revealed significantly higher H3K18la levels in recurrent HCC tissues after IMWA than in those after surgical resection (Fig. 3I). These data suggest that post-IMWA HCC is characterized by upregulated H3K18la expression. From an epigenetic perspective, the increased expression and enrichment of H3K18la in promoter regions may play a crucial role in driving the expression of target genes (Fig. 3J).

3.4. H3K18a drives the upregulation of NFS1 expression to suppress ferroptosis in heat-treated HCC

To comprehensively elucidate the mechanisms by which sublethal HS, lactate, and H3K18la promote HCC progression, we employed a multiomics approach to explore functional candidate genes (Fig. 4A). First, we conducted a joint analysis of transcriptomic and proteomic data to identify signature biomarkers and pathways affected by sublethal HS. A total of 7752 out of 9697 protein-coding transcripts were detected at the protein level, indicating comprehensive coverage of the proteomic dataset (Fig. 4B). The expression of mRNAs was positively correlated with protein expression, as demonstrated by Spearman correlation analysis (Fig. 4C). Through gene annotation analysis, we identified genes exhibiting high quantification values and frequent detection that were associated with the biological process of intracellular iron ion homeostasis. Similarly, genes involved in the molecular function of iron ion binding were also significantly enriched in heat-treated HCC cells (Fig. 4D). KEGG pathway analysis revealed that the ferroptosis pathway was significantly enriched in representative upregulated DEGs (Fig. 4E). Notably, the genes associated with platinum drug resistance were found to be significantly enriched, as evidenced by both the transcriptome and proteome databases (Fig. 4E and F).

Resistance to ferroptosis plays a crucial role in chemotherapy resistance to platinum drugs in colorectal cancer [23]. To investigate whether anti-ferroptosis and platinum resistance are involved in the progression of sublethal HS HCC, we searched FerrDb, a public ferroptosis gene database (http://www.zhounan.org/ferrdb), and conducted an integrated analysis using the transcriptome and proteome data. Among genes exhibiting absolute Pearson's correlation coefficients (CCs) exceeding 0.5, the representative anti-ferroptosis genes SLC7A11 and GSS demonstrated a negative association between RNA and protein expression levels. Moreover, a positive correlation was observed between the RNA and protein expression of the iron-sulfur cluster synthesis genes ISCU and NFS1, as well as the core anti-ferroptosis gene GPX4, with respective CCs of 0.905, 0.619, and 0.5 (Fig. 4G). To determine the potential functional significance of H3K18la, we performed ChIP-seq using anti-H3K18la antibodies to identify candidate genes. We identified 1050 increased H3K18la binding peaks in the HS group, 4.51 % (47 upregulated genes) of which were located in promoter sequences (±3 kb to the transcriptional start sites) (Fig. 4H). KEGG analysis revealed that the upregulated genes in the sublethal HS group were enriched in pathways related to cancer metastasis (Fig. 4I). Furthermore, we analyzed the overlapping upregulated genes across the transcriptomic, proteomic, and ChIP-seq databases and identified eleven candidate genes (Fig. 4J). We subsequently validated the expression of these genes, along with representative ferroptosis genes. Notably, the expression of the iron–sulfur cluster synthesis gene NFS1 was significantly upregulated (Fig. 4K and L). In addition, ChIP-seq data revealed that H3K18la was enriched at the promoter of NFS1 in heat-treated HCC cells (Fig. 4M). However, H3K18la was not significantly enriched at the promoter regions of other ferroptosis genes, including GPX4, ATF4, GSS, and ISCU (Supplementary Fig. 3 A-D).

3.5. NFS1 is required for HCC metastasis under sublethal HS

We analyzed the expression of NFS1 under sublethal HS. RT–qPCR and Western blotting confirmed the increased expression of NFS1 in HCC cells treated with sublethal HS (Fig. 5A and B). Additionally, we performed IHC staining using both HCC CDX mouse model and patient samples, revealing the significant upregulation of NFS1 expression after IMWA (Fig. 5C and D). To elucidate the link between the lactate-induced increase in NFS1 overexpression, HCC cells were incubated with 0, 5 or 10 mM lactate for 2 days. As expected, treatment with lactate sufficiently increased NFS1 expression (Fig. 5E). In addition, immunoblot assays demonstrated that the depletion of LDHA decreased the expression of NFS1 in HCC cells treated at both 37 °C and 47 °C (Fig. 5F). Collectively, the aforementioned evidence suggests that intracellular lactate levels have a significant effect on the expression of NFS1.

NFS1 is essential for the initiation of metastatic lung tumors [31]. We therefore investigated whether NFS1 also plays a role in mediating the metastatic potential of HCC cells. We silenced NFS1 with 2 short hairpin RNAs (shNfs1#1 and shNfs1#2) in MHCC-97H and Huh7 cells. shNfs1#1 induced a significant reduction in the expression of NFS1 and thus was utilized in subsequent investigations (Fig. 5G). The downregulation of NFS1 expression may lead to impaired cellular viability and diminished anti-toxic capacity [23]. We performed cell viability and cytotoxicity assays to evaluate the impact of NFS1 inhibition on HCC cells. IF staining and flow cytometry analyses demonstrated that the inhibition of NFS1 markedly compromised the viability of HCC cells, affecting not only those treated at 47 °C but also those maintained at 37 °C (Fig. 5H and Supplementary Fig. 4A). We subsequently investigated the role of NFS1 in HCC metastasis by conducting transwell assays. Silencing NFS1 diminished the sublethal HS-induced increase in the metastatic potential of HCC cells (Fig. 5I and Supplementary Fig. 4B). Consistently, in the tail vein injection animal model, NFS1 knockdown reduced pulmonary metastasis in both heat-treated and untreated MHCC-97H cells (Fig. 5J and K). To investigate the influence of NFS1 on EMT potential, we examined the expression of EMT markers by Western blot analysis in HCC cells with or without HS treatment. The expression of N-cadherin and vimentin significantly decreased after silencing NFS1; no noticeable change in E-cadherin expression was observed (Fig. 5L). These findings collectively suggest that the downregulation of NFS1 expression effectively impedes sublethal HS-induced HCC metastasis.

3.6. Upregulation of Nfs1 expression reduces susceptibility to ferroptosis after sublethal HS

NFS1 harvests sulfur from cysteine for the biosynthesis of iron–sulfur clusters and protects cells from ferroptosis [17]. When the assembly of these clusters is disrupted due to reduced NFS1 expression, cells may initiate an "iron-starvation response", ultimately leading to ferroptosis [32]. To elucidate the mechanism by which NFS1 promotes HS HCC metastasis, we examined the functional alterations resulting from NFS1

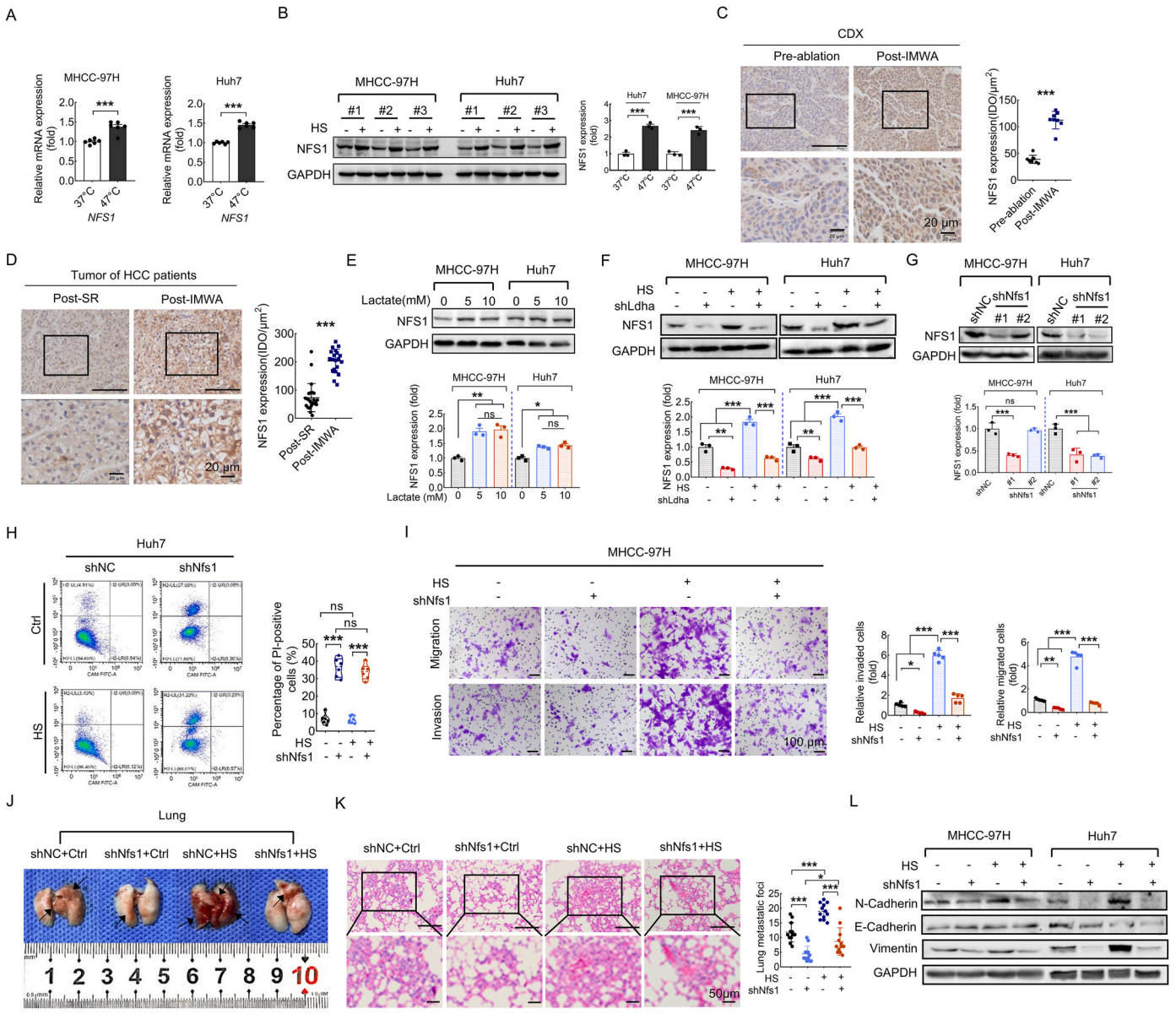

Fig. 5. NFS1 is required for HCC metastasis under sublethal HS. (A) The mRNA level of NFS1 in MHCC-97H or Huh7 cells treated at 37 °C or 47 °C. (B) Representative Western blot images and quantification of NFS1 following exposure to 37 °C or 47 °C. (C) IHC staining of NFS1 in CDX sections from the mouse model before and after IMWA. Scale bar, 20 μm. (D) IHC staining showing the expression of NFS1 in HCC samples from patients following SR or IMWA. Scale bar, 20 μm. (E) Immunoblot and quantification analyses of NFS1 in HCC cells incubated with 0, 5, or 10 mM lactate after being subjected to either a 47 °C or 37 °C water bath. (F) Immunoblots showing the expression of NFS1 in shNC- and shLdha-transfected HCC cells, with or without sublethal HS. (G) Representative immunoblot images and quantification of NFS1 in MHCC-97H and Huh7 cells transfected with shNC or shNfs1. (H) Flow cytometry analysis showing the dampening effects of NFS1 on Huh7 cells treated at 37 °C or 47 °C. (I) Transwell assay illustrating the migration and invasion abilities of MHCC-97H cells transfected with shNC or shNfs1, with or without exposure to sublethal HS. Scale bar, 100 μm. (J, K) The evaluation of lung metastasis in mice four weeks after the intravenous injection of MHCC-97H cells infected with shNC or shNfs1, followed by treatment with sublethal HS or at the control temperature, was conducted through macroscopic observations and histological analysis via H&E staining. Scale bar, 50 μm. (L) Representative Western blot images and quantification of EMT-related markers in shNC- or shLdha-transfected HCC cells with or without sublethal HS. See Supplementary Fig. 4 for supplementary data.

depletion. Principal component analysis revealed significant differences in gene profiles between shNC and shNfs1 heat-treated HCC cells (Fig. 6A), with 3201 downregulated genes and 3415 upregulated genes observed in the shNfs1 group compared with the shNC group (Fig. 6B and C). The downregulated genes in the GO categories were significantly suppressed in terms associated with cell motility and cytoskeletal assembly (Fig. 6D). Moreover, sublethal heat-treated HCC cells exhibited a compromised drug metabolism capacity in the presence of NFS1 silencing (Fig. 6E). Notably, NFS1 depletion attenuated the expression of genes involved in platinum resistance, as well as the stress response (Fig. 6F). NFS1 plays a critical role in the biosynthesis of iron–sulfur clusters; as anticipated, the inhibition of NFS1 significantly hampered the activation of genes involved in 2 iron, 2 sulfur cluster (2Fe–2S) binding (Fig. 6G). The GPX4 protein plays a pivotal role in inhibiting ferroptosis by eliminating phospholipid hydroperoxide [33]. Unlike GPX4, the modulation of ferroptosis by ATF4 plays a dual role depending on its target genes [34]. Therefore, we assessed the expression of GPX4 and ATF4 in shNC- and shNfs1-transfected HCC cells, both with and without sublethal HS treatment. Immunoblotting revealed that GPX4 was overexpressed in heat-treated Huh7 cells regardless of NFS1 inhibition. ATF4 expression in HCC cells was upregulated upon NFS1 depletion or HS treatment. Additionally, the expression levels of key

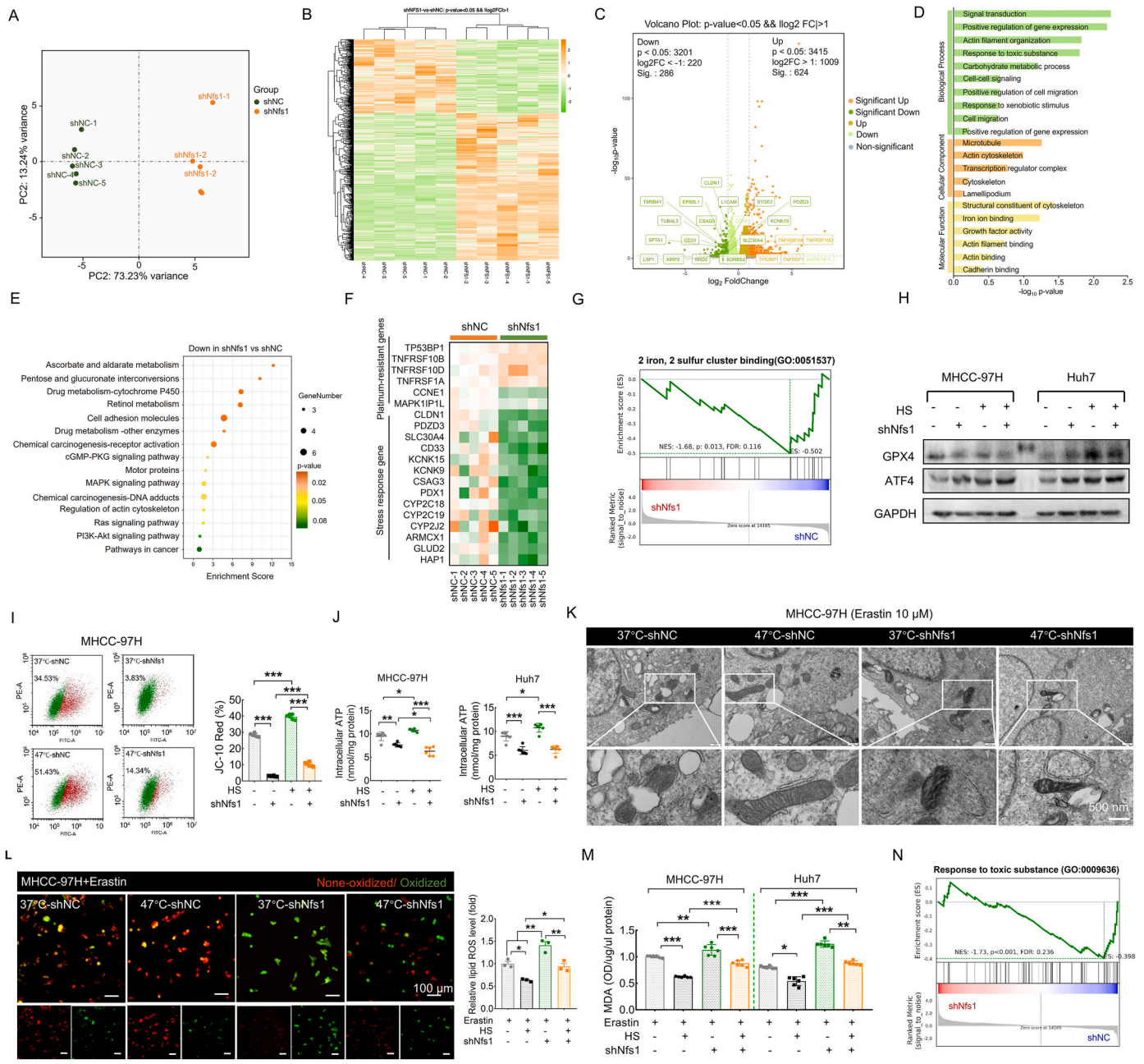

Fig. 6. Upregulation of NFS1 expression reduces susceptibility to ferroptosis after sublethal HS. (A) Principal component analysis (PCA) of shNC- and shNfs1-transfected HS HCC cells on the basis of transcriptome sequencing data. (B) Heatmap illustrating the differential gene expression in heat-treated HCC cells following NFS1 knockdown. (C) Volcano plot of the transcriptomic analysis of shNC- vs. shNfs1-transfected HS HCC cells. Significantly increased and decreased protein levels are indicated by orange and green dots, respectively (n = 5 per group). (D) GO enrichment analysis revealed downregulated GO terms following NFS1 knockdown. (E) Bubble chart illustrating the suppressed KEGG pathways in sublethal heat-treated HCC cells transfected with shNfs1. (F) The expression of genes related to the stress response and platinum resistance. (G) Gene set enrichment analysis (GSEA) showing the downregulated genes involved in the 2 iron, 2 sulfur cluster (H) Western blot images of the expression of NFS1, the ferroptosis marker GPX4, and ARF4 in HCC cells transfected with shNC or shNfs1 and treated at either 37 °C or 47 °C. (I) Cytometric analysis of the mitochondrial membrane potential (ΔΨm) in MHCC-97H cells transfected with shNC or shNfs1, with or without exposure to sublethal amounts of HS. Scale bar, 10 μm. (J) Intracellular ATP levels in shNC- and shNfs1-transfected HCC cells exposed to 37 °C or 47 °C. (K) Representative transmission electron microscopy images of HCC cells incubated with 10 μM erastin. Scale bar, 500 nm. (L) C11-BODIPY staining revealed that lipid ROS levels were higher in shNfs1-HCC cells than in shNC-treated cells, regardless of the presence of sublethal HS. Scale bar, 100 μm. (M) The levels of malondialdehyde induced by erastin in HCC cells transfected with shNC or shNfs1 and treated with or without sublethal HS. (N) Gene set enrichment analysis (GSEA) showing the downregulated genes associated with the response to toxic substances. See Supplementary Fig. 5 for supplementary data.

ferroptosis-associated genes, including PTGS2, TRFC, and ACO1, were compared between shNC and shNfs1 HCC cells treated with or without HS (Supplementary Fig. 5A).

The metabolic activities of mitochondria, including both the tricarboxylic acid (TCA) cycle and mitochondrial electron transport chain (ETC) activity, are indispensable for generating an adequate amount of lipid reactive oxygen species (ROS) to initiate ferroptosis [34]. The occurrence of ferroptosis is concomitant with impaired mitochondrial function, characterized by reductions in both ATP synthesis and the membrane potential [35]. Therefore, we utilized JC-10 to assess the

mitochondrial membrane potential (ΔΨm) and evaluate mitochondrial functionality. Compared with that of the MHCC-97H cells treated at 37 °C, the ΔΨm of the MHCC-97H cells exposed to sublethal HS was significantly higher. However, in the shNfs1 group, the ΔΨm consistently decreased regardless of HS exposure (Fig. 6I and Supplementary Fig. 5B). Compared with the 37 °C group, the sublethal heat-treated HCC cells presented an increase in ATP production, a finding that was consistent with the alteration in ΔΨm. shNfs1-transfected HCC cell lines cultured at 37 °C and 47 °C presented significant decreases in ATP levels (Fig. 6J). Erastin, a well-established inhibitor of the glutamate/cystine antiporter (system Xc-) that triggers ferroptosis, was subsequently utilized to test our hypothesis regarding the potential mitigation of susceptibility to ferroptosis through increased NFS1 expression [36]. We used transmission electron microscopy to observe the mitochondrial morphology of HCC cells treated with 10 μM erastin. Erastin-induced ferroptosis was characterized by a reduction in mitochondrial size, distorted cristae, and decreased crista density, particularly after NFS1 depletion (Fig. 6K). Lipid peroxidation is a hallmark of ferroptosis that directly damages cellular membranes and thus induces ferroptosis [37]. The accumulation of lipid ROS was analyzed using C11-BODIPY, a fluorescent probe utilized for the detection of lipid oxidation. We observed that sublethal HS conferred protection against the erastin-induced accumulation of lipid ROS in HCC cells and that NFS1 depletion synergistically enhanced the pro-ferroptotic effects of erastin (Fig. 6L). Additionally, the treatment of HCC cells at 47 °C resulted in a reduction in the levels of malondialdehyde (MDA), a byproduct generated during lipid peroxidation; however, this effect was reversed in shNfs1 HCC cells (Fig. 6M). The genes associated with the cellular response to toxic substances were found to be compromised in sublethal HS HCC cells, a result that is consistent with the aforementioned findings (Fig. 6N). Moreover, the expression of genes associated with cellular motility and metastasis was downregulated after the knockdown of NFS1 (Supplementary Fig. 5C).

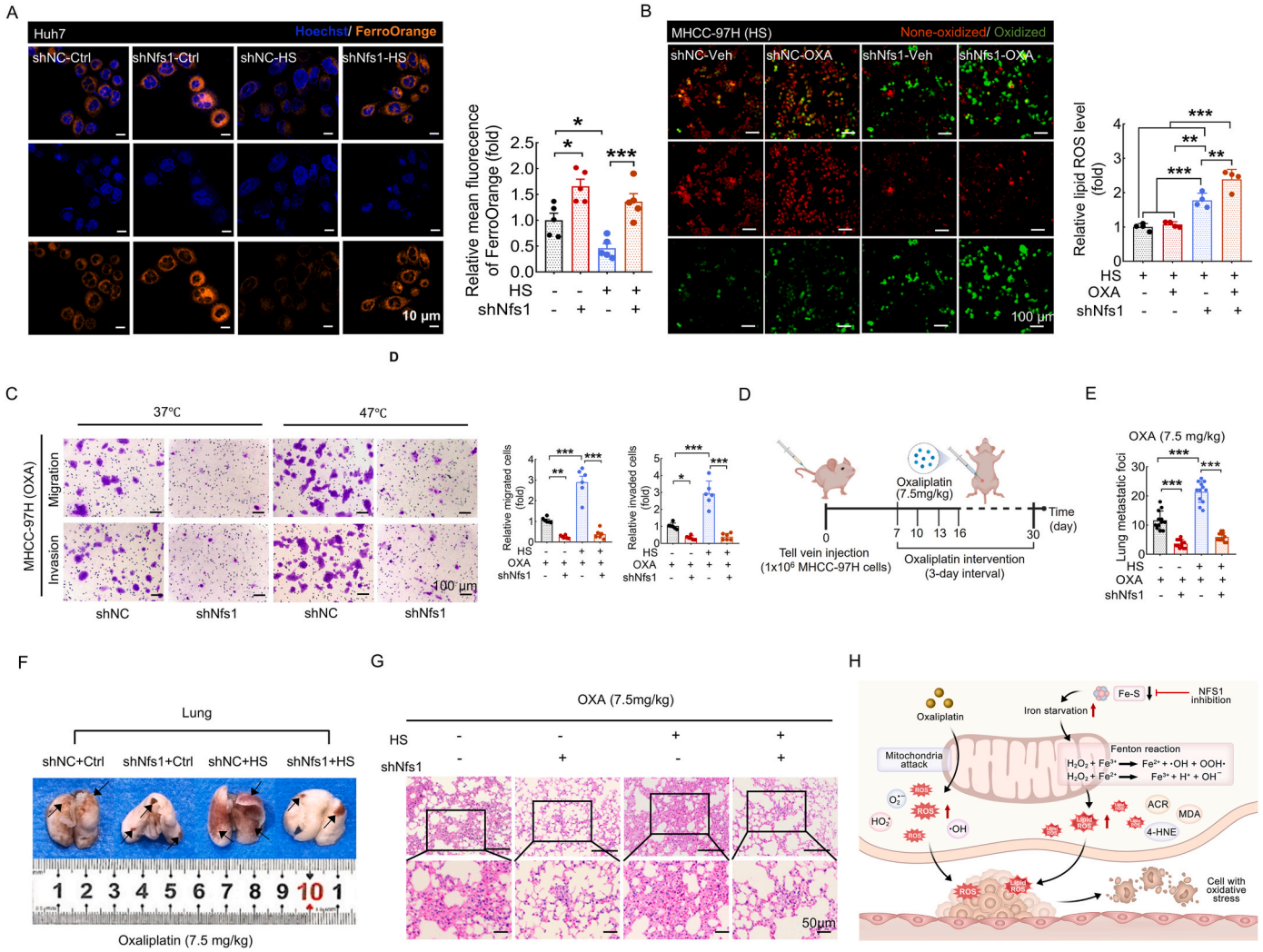

Fig. 7. NFS1 knockdown enhances the inhibitory effect of oxaliplatin (OXA) treatment on HCC metastasis. (A) Immunofluorescence (IF) staining showing that the decrease in cellular Fe^{2+} levels induced by sublethal HS was reversed upon NFS1 ablation in both control and heat-treated Huh7 cells. Scale bar, 10 μm. (B) The combination of NFS1 knockdown and OXA treatment effectively suppressed cellular lipid ROS production in both control and heat-treated MHCC-97H cells, as shown by C11-BODIPY staining. Scale bar, 100 μm. (C) Transwell assay showing the metastatic capability of HCC cells transfected with shNC or shNfs1 and treated at 37 °C or 47 °C. Scale bar, 100 μm. (D) Schematic representation of the mouse model generated by the intravenous injection of MHCC-97H cells transfected with either shNC or shNfs1 via the caudal vein, accompanied by the intraperitoneal administration of 7.5 mg/kg OXA every three days until day 30. (E–G) Quantitative analysis (E) and representative macroscopic (F) and H&E staining (G) images of lung metastases in mice 30 days after tail vein injection of HCC cells combined with OXA treatment. Scale bar, 50 μm. (H) Diagram illustrating the hypothetical synergistic interaction between OXA and NFS1 inhibition, potentially augmenting anti-HCC efficacy by increasing ROS production. See Supplementary Fig. 6 for supplementary data.

3.7. NFS1 knockdown enhances the inhibitory effect of OXA treatment against HCC metastasis

The production of ROS in malignant cells has been reported as a fundamental mechanism underlying the synergistic cytotoxic effects observed in combination anticancer therapies [38]. Elevated NFS1 expression has been shown to be associated with poor survival and hyposensitivity to OXA-based chemotherapy in patients diagnosed with colorectal cancer [23]. Considering the ability of OXA to impede cancer progression by increasing intracellular ROS production, we postulate

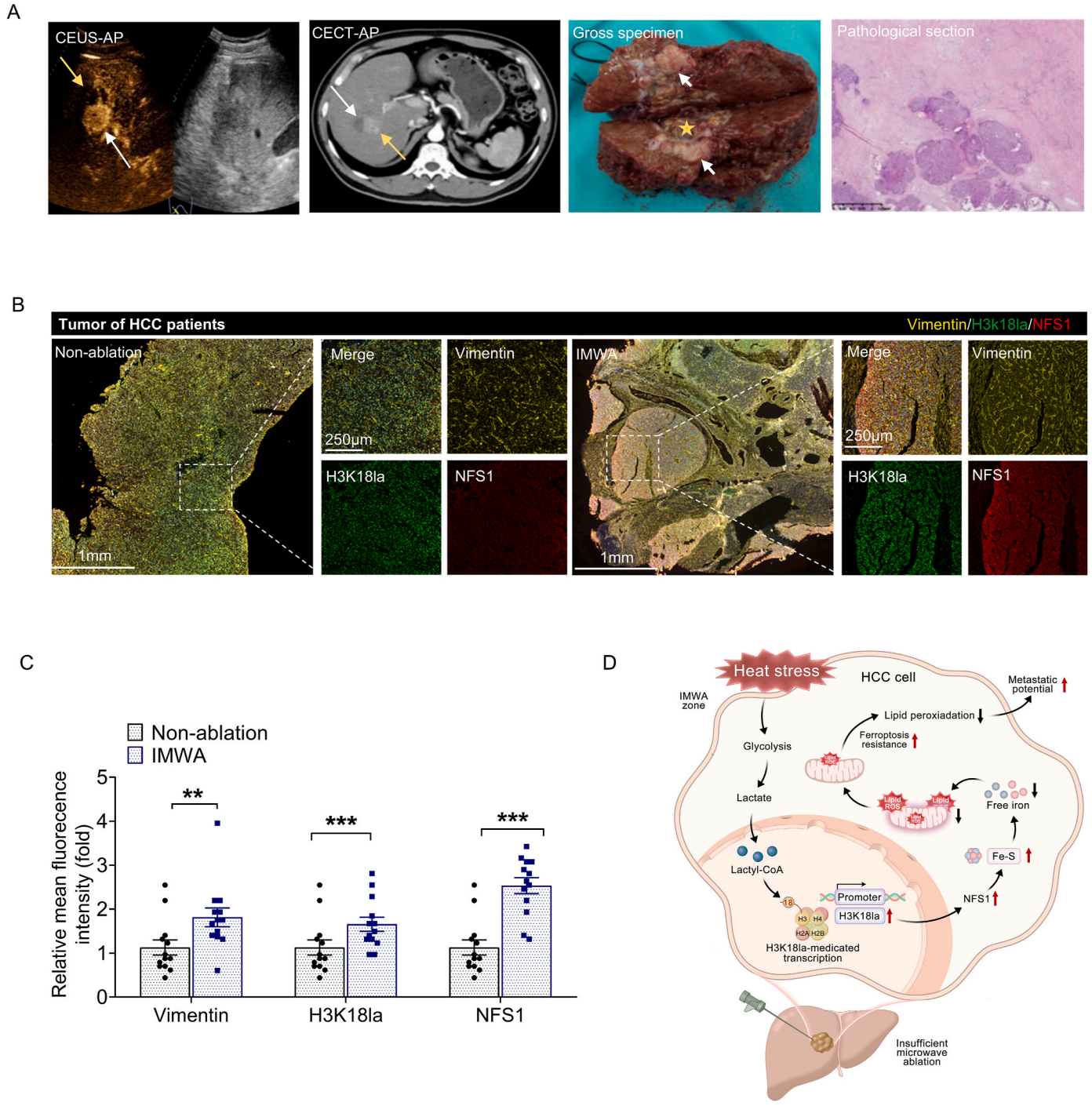

Fig. 8. The H3K18/NFS1 pathway mediates the increase in the metastatic capacity of HCC cells subjected to sublethal HS. (A) Representative imaging of and pathological results for patients with HCC. Suspicious enhanced areas were detected beside treated regions after microwave ablation via contrast-enhanced ultrasound and CT (left two images) in the arterial phase (AP). Abnormal enhanced areas were diagnosed as recurrent HCC in situ via histopathology after surgical resection (right two images). (B, C) Representative fluorescence microscopy images and quantitative analysis of H3K18la (green), NFS1 (red), and vimentin (yellow) expression in HCC sections of recurrent tumors in situ after surgical resection and microwave ablation treatment. Scale bar, 1 mm. (D) A schematic diagram illustrating the mechanism by which sublethal heat shock increases the metastatic potential of HCC. The sublethal HS response increases glycolysis and intracellular lactate production, influencing overall H3K18la levels. H3K18la is significantly enriched at the promoter region of NFS1, a gene essential for iron–sulfur cluster biosynthesis, resulting in reduced free iron levels and decreased lipid peroxidation. This process enhances the resistance of HCC cells to ferroptosis, thereby promoting their metastatic potential.

that its synergistic interaction with NFS1 downregulation could augment anticancer efficacy via an amplified ROS response. The iron-starvation reaction is characterized by the excessive accumulation of iron, particularly in the form of ferrous iron (Fe^{2+}) [32]. Therefore, we assessed the overall cellular Fe^{2+} levels via FerroOrange staining. Compared with cells maintained at 37 °C, HCC cells exposed to sublethal HS presented lower levels of cellular ferrous iron. Conversely, the shNfs1 groups presented higher levels of cellular ferrous iron, both with and without HS treatment (Fig. 7A and Supplementary Fig. 6). To study the synergistic impact of NFS1 on HCC cells, sublethal heat-treated MHCC-97H cells were treated with 5 μM OXA. The IF staining results demonstrated that OXA treatment alone did not significantly increase lipid ROS levels, whereas the combination of OXA and Nfs1 knockdown resulted in a 2.4-fold increase in lipid ROS levels (Fig. 7B). To ascertain the superior inhibitory effects offered by combination therapy, the metastatic potential of HCC cells was evaluated both in vitro and in vivo. Transwell assays demonstrated that OXA moderately inhibited the migratory and invasive abilities of HCC cells. However, in combination with NFS1 deficiency, OXA treatment significantly impaired the metastatic potential of HCC cells, regardless of exposure to sublethal HS (Fig. 7C). Furthermore, an animal model was established by injecting MHCC-97H cells transfected with either shNC or shNfs1 into each mouse via the caudal vein. OXA was administered intraperitoneally at a dosage of 7.5 mg/kg every three days until day 30 (Fig. 7D). The promotion of lung metastasis in HCC cells by HS was observed even after OXA administration in the shNC group. However, knocking down NFS1 significantly reduced lung metastasis regardless of HS (Fig. E–G). Taken together, the data presented herein demonstrate a pronounced synergistic effect between NFS1 knockdown and OXA treatment in suppressing HCC metastasis (Fig. 7H).

3.8. The H3K18/NFS1 pathway mediates the increase in the metastatic capacity of HCC cells after IMWA

We investigated the expression of H3K18la, NFS1, and vimentin in clinical HCC samples. Suspected in situ recurrence after microwave treatment for primary HCC was detected through imaging and subsequently surgically resected and confirmed as recurrent HCC by histopathology (Fig. 8A). Through IF staining, we observed higher levels of H3K18la, NFS1, and vimentin in recurrent HCC tissue after IMWA than in surgically resected HCC tissue (Fig. 8B and C).

4. Discussion

Our study demonstrated that the metastatic potential of HCC increased in a lactate-dependent manner after IMWA. We presented evidence demonstrating that HCC cells exhibit enhanced intracellular iron ion homeostasis and increased resistance to platinum drugs after exposure to sublethal HS. Mechanistically, sublethal heat stress triggers an increase in H3K18la modification, which in turn enhances the transcriptional activity of NFS1, a key enzyme in iron-sulfur cluster biosynthesis. Elevated NFS1 expression subsequently reduces the susceptibility of HCC cells to ferroptosis. To our knowledge, this is the first report of the epigenetic modulation of ferroptosis during HCC progression after IMWA. We bridge histone lactylation with ferroptosis, providing novel therapeutic targets for treating HCC following microwave ablation, particularly when combined with OXA-based chemotherapy.

Enhanced glycolysis and lactate accumulation are common features of various types of cancer [36]. Lactate, a major metabolite of glycolysis, is involved, in a variety of ways, in the progression of cancer; it not only serves as the carbon source for membrane lipid biosynthesis but also participates in the production of lipid substances and mediates ferroptosis [39]. In addition, high serum lactate dehydrogenase levels are associated with decreased survival in HCC patients after sorafenib treatment [40]. After being subjected to sublethal HS, HCC cells present significant metabolic alterations characterized by increased lactate production [8]. By both exogenously administering lactate and inhibiting endogenous lactate production, our study demonstrated that an increase in lactate facilitated the metastasis of HCC after IMWA. A lactate-rich microenvironment is a key driver of lactylation, potentially enhancing lactylation modifications across the tumor microenvironment, including parenchymal, stromal, and immune cells. Stimulation induced by environmental stresses on HCC cells leads to significant changes in gene transcription, translation, and post-translational modification of proteins [29,41]. Heat stress induced by thermal treatment may remodel the tumor microenvironment (TME), including tumor-specific immune response. Leuchte et al. revealed that a stronger IFN-γ and IL-5 T cell response against tumor-associated antigens correlates with longer remission and extended progression-free survival after MWA in HCC patients [42]. However, sublethal heat stress may also induce resistance to immune therapy; for example, residual HCC after insufficient radiofrequency ablation exhibit accelerated progression and anti-PD-1 resistance [30]. It is reported that lactate promotes tumor growth by enhancing MOESIN lactylation and TGF-β signaling, increasing Treg production, while combining PD-1 therapy with lactate dehydrogenase inhibitors boosts anti-tumor effects [43]. Therefore, targeting the interplay between lactylation, MWA treatment, and tumor microenvironment remodeling holds promising prognostic value for HCC patients.

Comprehensive lactylome analysis has suggested a lactylation-dependent mechanism of metabolic adaptation in HCC [14]. Histone lactylation in HCC was reported to predominantly occur on histones H2 and H1, with minimal variation observed between tumor tissues and adjacent liver tissues [14]. However, our study, revealed a significant increase in H3K18la levels following sublethal HS, which may be implicated in pathways associated with HCC progression, including the activation of gene expression by hepatic stellate cells [44]. The present study demonstrates that H3K18la enhances the transcriptional activity of NFS1, thereby mediating the anti-ferroptotic effects in HCC after IMWA. Recently, growing evidence suggests that ferroptosis may play a crucial role in MWA-induced tumor suppression through various mechanisms [45]. However, NFS1-mediated anti-ferroptosis in HCC progression following MWA treatment has not been reported. The NFS1 gene encodes the protein NFS1 cysteine desulfurase, which extracts sulfur from cysteine for the biosynthesis of iron–sulfur clusters. This process plays a crucial role in protein synthesis and various biological processes, including DNA repair, respiratory chain activity, nucleotide metabolism and cellular iron regulation [46]. Analyses of datasets from The Cancer Genome Atlas revealed that NFS1 expression was higher in several solid cancers than in noncancerous tissues. NFS1 suppression alone did not decrease glutathione levels or induce ferroptosis. However, NFS1 suppression has been shown to induce an iron starvation response, increasing cell vulnerability to ferroptosis, especially when reactive oxygen species (ROS) accumulate [47]. This finding is consistent with our findings in HCC cells. ROS play a crucial part in various processes of cell death including ferroptosis [48]. Cellular and organelle membranes are highly susceptible to ROS accumulation, leading to a process known as “lipid peroxidation,” which serves as a key driver of ferroptosis. The buildup of oxidized lipids compromises membrane integrity, ultimately resulting in iron-dependent cell death [48]. Erastin, an inhibitor of glutamate/cystine antiporters—channels responsible for maintaining intracellular glutathione levels—was applied, and a significant increase in lipid peroxidation was observed in shNfs1-transfected HCC cells. Thus, we concluded that sublethal HS increased the expression of NFS1 and protected HCC cells from erastin-induced ferroptosis. Notably, sublethal HS increased the expression of other antiferroptosis enzymes, such as GPX4 and ATF4, indicating that the regulation of sublethal HS is not only based on NFS1 but also on multiple pathways and genes. Importantly, the specific mechanisms involved need to be further investigated.

Approximately 54 % of HCC patients have little or no response to

OXA-based therapy [20]. During chemotherapy, some cancer cells can survive through numerous defense mechanisms. There are reports on the molecular mechanisms that confer OXA resistance in HCC cells, a process that has been shown to involve glucose metabolism, long noncoding RNA, methylation, etc [49–51]. The modulation of ferroptosis might contribute to decreasing OXA resistance [52,53]. In a chemotherapy study, lysyl-oxidase 3 inhibition in combination with OXA treatment inhibited HCC progression by inducing ferroptosis, improving the antitumor efficacy of OXA and decreasing chemotherapeutic toxicity [54]. We also found that the combination of OXA and NFS1 knockdown further enhanced lipid peroxidation in HCC cells and suppressed tumor metastasis. The findings suggest that NFS1 may serve as a promising therapeutic target for OXA-based chemotherapy in the treatment of HCC.In summary, we demonstrated that sublethal HS reduced the susceptibility of HCC cells to ferroptosis by inducing H3K18la modification-mediated upregulation of NFS1 expression, thereby promoting HCC metastasis. In vivo and in vitro, the silencing of NFS1 synergistically increased the effectiveness of OXA in treating HCC (Fig. 8D). Further research is imperative to bridge existing gaps in knowledge and deepen our understanding of the underlying mechanisms involved.

CRediT authorship contribution statement

Jiayan Huang: Investigation, Methodology, Resources, Software, Writing – original draft, Writing – review & editing. **Huijing Xie:** Data curation, Formal analysis, Writing – original draft. **Ju Li:** Methodology, Project administration. **Xiaotong Huang:** Formal analysis, Methodology, Software. **Yunshi Cai:** Formal analysis, Investigation, Methodology. **Rui Yang:** Methodology, Software. **Dongmei Yang:** Formal analysis. **Wuyongga Bao:** Resources. **Yongjie Zhou:** Conceptualization, Methodology. **Tao Li:** Conceptualization, Writing – review & editing. **Qiang Lu:** Conceptualization, Funding acquisition, Methodology.

Data availability

Microarray data were deposited in NCBI Gene Expression Omnibus (GEO, GSE279569) and National Genomics Data Center (OMIX, OMIX007670). ChIP-Seq data can be request to contact the corresponding author. All data needed to evaluate the conclusions in the paper are present in the paper and/or the Supplementary Materials.

Ethics

The authors of this manuscript declare no relationships with any companies whose products or services may be related to the subject matter of the article. The authors of this manuscript conformed with the Helsinki Declaration of 1975, which was revised in 2008 concerning Human and Animal Rights, and they followed the policy concerning informed consent, as shown on Springer.com.

Funding

This study was supported in part by grants from the National Natural Science Foundation of China (82171952 and 82370260) and the Key Research and Development Program of Sichuan Province (22ZDYF2138).

Declaration of competing interest

The authors declare that they have no known competing financial interests or personal relationships that could have appeared to influence the work reported in this paper.

Acknowledgments

The authors sincerely appreciate Li Li, Fei Chen, Chunjuan Bao, and Yang Deng from the Institute of Clinical Pathology, West China Hospital. Sichuan University for processing histological staining. The authors gratefully acknowledge Yan Wang and Xiangyi Ren from the Core Facilities, West China Hospital, Sichuan University for their assistance and guidance for their technical assistance and guidance.

Appendix A. Supplementary data

Supplementary data to this article can be found online at https://doi.org/10.1016/j.redox.2025.103553.

References

[1] H. Sung, J. Ferlay, R.L. Siegel, et al., Global cancer statistics 2020: GLOBOCAN estimates of incidence and mortality worldwide for 36 cancers in 185 countries, CA Cancer J. Clin. 71 (3) (2021) 209–249.
[2] J. Zhou, H. Sun, Z. Wang, et al., Guidelines for the diagnosis and treatment of hepatocellular carcinoma (2019 edition), Liver Cancer 9 (6) (2020) 682–720.
[3] J.K. Heimbach, L.M. Kulik, R.S. Finn, et al., AASLD guidelines for the treatment of hepatocellular carcinoma, Hepatology 67 (1) (2018) 358–380.
[4] J. Yu, Z.G. Cheng, Z.Y. Han, et al., Period-dependent survival benefit of percutaneous microwave ablation for hepatocellular carcinoma: a 12-year real-world, multicentric experience, Liver Cancer 11 (4) (2022) 341–353.
[5] S. Yoshida, M. Kornek, N. Ikenaga, et al., Sublethal heat treatment promotes epithelial-mesenchymal transition and enhances the malignant potential of hepatocellular carcinoma, Hepatology 58 (5) (2013) 1667–1680.
[6] D.E. Jondal, S.M. Thompson, K.A. Butters, et al., Heat stress and hepatic laser thermal ablation induce hepatocellular carcinoma growth: role of PI3K/mTOR/AKT signaling, Radiology 288 (3) (2018) 730–738.
[7] W.H. Koppenol, P.L. Bounds, C.V. Dang, Otto Warburg's contributions to current concepts of cancer metabolism, Nat. Rev. Cancer 11 (5) (2011) 325–337.
[8] Y. Chen, J. Bei, M. Liu, et al., Sublethal heat stress-induced O-GlcNAcylation coordinates the Warburg effect to promote hepatocellular carcinoma recurrence and metastasis after thermal ablation, Cancer Lett. 518 (2021) 23–34.
[9] F. Yang, L. Hilakivi-Clarke, A. Shaha, et al., Metabolic reprogramming and its clinical implication for liver cancer, Hepatology 78 (5) (2023) 1602–1624.
[10] D. Du, C. Liu, M. Qin, et al., Metabolic dysregulation and emerging therapeutical targets for hepatocellular carcinoma, Acta Pharm. Sin. B 12 (2) (2022) 558–580.
[11] D. Zhang, Z. Tang, H. Huang, et al., Metabolic regulation of gene expression by histone lactylation, Nature 574 (7779) (2019) 575–580.
[12] J. Yu, P. Chai, M. Xie, et al., Histone lactylation drives oncogenesis by facilitating m(6)A reader protein YTHDF2 expression in ocular melanoma, Genome Biol. 22 (1) (2021) 85.
[13] J. Yang, L. Luo, C. Zhao, et al., A positive feedback loop between inactive VHL-triggered histone lactylation and PDGFRβ signaling drives clear cell renal cell carcinoma progression, Int. J. Biol. Sci. 18 (8) (2022) 3470–3483.
[14] Z. Yang, C. Yan, J. Ma, et al., Lactylome analysis suggests lactylation-dependent mechanisms of metabolic adaptation in hepatocellular carcinoma, Nat. Metab. 5 (1) (2023) 61–79.
[15] L. Pan, F. Feng, J. Wu, et al., Demethylzeylasteral targets lactate by inhibiting histone lactylation to suppress the tumorigenicity of liver cancer stem cells, Pharmacol. Res. 181 (2022) 106270.
[16] X. Jiang, B.R. Stockwell, M. Conrad, Ferroptosis: mechanisms, biology and role in disease, Nat. Rev. Mol. Cell Biol. 22 (4) (2021) 266–282.
[17] S.W. Alvarez, V.O. Sviderskiy, E.M. Terzi, et al., NFS1 undergoes positive selection in lung tumours and protects cells from ferroptosis, Nature 551 (7682) (2017) 639–643.
[18] Y. Pang, G. Tan, X. Yang, et al., Iron-sulphur cluster biogenesis factor LYRM4 is a novel prognostic biomarker associated with immune infiltrates in hepatocellular carcinoma, Cancer Cell Int. 21 (1) (2021) 463.
[19] M. He, Q. Li, R. Zou, et al., Sorafenib plus hepatic arterial infusion of oxaliplatin, fluorouracil, and leucovorin vs sorafenib alone for hepatocellular carcinoma with portal vein invasion: a randomized clinical trial, JAMA Oncol. 5 (7) (2019) 953–960.
[20] Q.J. Li, M.K. He, H.W. Chen, et al., Hepatic arterial infusion of oxaliplatin, fluorouracil, and leucovorin versus transarterial chemoembolization for large hepatocellular carcinoma: a randomized phase III trial, J. Clin. Oncol. 40 (2) (2022) 150–160.
[21] N. Lyu, Y. Kong, L. Mu, et al., Hepatic arterial infusion of oxaliplatin plus fluorouracil/leucovorin vs. sorafenib for advanced hepatocellular carcinoma, J. Hepatol. 69 (1) (2018) 60–69.
[22] Y. Shi, Y. Niu, Y. Yuan, et al., PRMT3-mediated arginine methylation of IGF2BP1 promotes oxaliplatin resistance in liver cancer, Nat. Commun. 14 (1) (2023) 1932.
[23] J.F. Lin, P.S. Hu, Y.Y. Wang, et al., Phosphorylated NFS1 weakens oxaliplatin-based chemosensitivity of colorectal cancer by preventing PANoptosis, Signal Transduct. Targeted Ther. 7 (1) (2022) 54.

[24] T. Su, J. Liao, Z. Dai, et al., Stress-induced phosphoprotein 1 mediates hepatocellular carcinoma metastasis after insufficient radiofrequency ablation, Oncogene 37 (26) (2018) 3514–3527.
[25] W.C. Mah, T. Thurnherr, P.K. Chow, et al., Methylation profiles reveal distinct subgroup of hepatocellular carcinoma patients with poor prognosis, PLoS One 9 (8) (2014) e104158.
[26] O.V. Grinchuk, S.P. Yenamandra, R. Iyer, et al., Tumor-adjacent tissue co-expression profile analysis reveals pro-oncogenic ribosomal gene signature for prognosis of resectable hepatocellular carcinoma, Mol. Oncol. 12 (1) (2018) 89–113.
[27] Y. Xu, X. Hao, Y. Ren, et al., Research progress of abnormal lactate metabolism and lactate modification in immunotherapy of hepatocellular carcinoma, Front. Oncol. 12 (2022) 1063423.
[28] Y.J. Hwang, J.S. Bae, Y. Lee, B.Y. Hur, D.H. Lee, H. Kim, Classification of microvascular invasion of hepatocellular carcinoma: correlation with prognosis and magnetic resonance imaging, Clin. Mol. Hepatol. 29 (3) (2023) 733–746.
[29] T. Su, M. Huang, J. Liao, et al., 2)(SI)Insufficient radiofrequency ablation promotes hepatocellular carcinoma metastasis through N6-methyladenosine mRNA methylation-dependent mechanism, Hepatology 74 (3) (2021) 1339–1356.
[30] X. Liu, W. Zhang, Y. Xu, et al., 1)(SI)Targeting PI3Kγ/AKT pathway remodels LC3-associated phagocytosis induced immunosuppression after radiofrequency ablation, Adv. Sci. 9 (7) (2022) e2102182.
[31] M. Tong, T.L. Wong, H. Zhao, et al., Loss of tyrosine catabolic enzyme HPD promotes glutamine anaplerosis through mTOR signaling in liver cancer, Cell Rep. 37 (5) (2021) 109976.
[32] E.M. Terzi, V.O. Sviderskiy, S.W. Alvarez, G.C. Whiten, R. Possemato, Iron-sulfur cluster deficiency can be sensed by IRP2 and regulates iron homeostasis and sensitivity to ferroptosis independent of IRP1 and FBXL5, Sci. Adv. 7 (22) (2021) eabg4302.
[33] Q. Xue, D. Yan, X. Chen, et al., Copper-dependent autophagic degradation of GPX4 drives ferroptosis, Autophagy 19 (7) (2023) 1982–1996.
[34] H. Tang, R. Kang, J. Liu, D. Tang, ATF4 in cellular stress, ferroptosis, and cancer, Arch. Toxicol. 98 (4) (2024) 1025–1041.
[35] C. Wu, W. Zhao, J. Yu, S. Li, L. Lin, X. Chen, Induction of ferroptosis and mitochondrial dysfunction by oxidative stress in PC12 cells, Sci. Rep. 8 (1) (2018) 574.
[36] W.S. Yang, B.R. Stockwell, Ferroptosis: death by lipid peroxidation, Trends Cell Biol. 26 (3) (2016) 165–176.
[37] J.Y. Lee, W.K. Kim, K.H. Bae, S.C. Lee, E.W. Lee, Lipid metabolism and ferroptosis, Biology (Basel). 10 (3) (2021) 184.
[38] W. Chen, W. Lian, Y. Yuan, M. Li, The synergistic effects of oxaliplatin and piperlongumine on colorectal cancer are mediated by oxidative stress, Cell Death Dis. 10 (8) (2019) 600.
[39] Y. Zhao, M. Li, X. Yao, et al., HCAR1/MCT1 regulates tumor ferroptosis through the lactate-mediated AMPK-SCD1 activity and its therapeutic implications, Cell Rep. 33 (10) (2020) 108487.
[40] L. Faloppi, M. Scartozzi, M. Bianconi, et al., The role of LDH serum levels in predicting global outcome in HCC patients treated with sorafenib: implications for clinical management, BMC Cancer 14 (2014) 110.
[41] G.P. Nagaraju, B. Dariya, P. Kasa, S. Peela, B.F. El-Rayes, Epigenetics in hepatocellular carcinoma, Semin. Cancer Biol. 86 (Pt 3) (2022) 622–632.
[42] K. Leuchte, E. Staib, M. Thelen, et al., Microwave ablation enhances tumor-specific immune response in patients with hepatocellular carcinoma, Cancer Immunol. Immunother. 70 (4) (2021) 893–907.
[43] J. Gu, J. Zhou, Q. Chen, et al., Tumor metabolite lactate promotes tumorigenesis by modulating MOESIN lactylation and enhancing TGF-β signaling in regulatory T cells, Cell Rep. 40 (3) (2022) 111122.
[44] H. Rho, A.R. Terry, C. Chronis, N. Hay, Hexokinase 2-mediated gene expression via histone lactylation is required for hepatic stellate cell activation and liver fibrosis, Cell Metab. 35 (8) (2023) 1406–1423.e8.
[45] L. Yu, M. Cheng, J. Liu, et al., Crosstalk between microwave ablation and ferroptosis: the next hot topic, Front. Oncol. 13 (2023) 1099731.
[46] O. Stehling, C. Wilbrecht, R. Lill, Mitochondrial iron-sulfur protein biogenesis and human disease, Biochimie 100 (2014) 61–77.
[47] S.C. Chafe, F.S. Vizeacoumar, G. Venkateswaran, et al., Genome-wide synthetic lethal screen unveils novel CAIX-NFS1/xCT axis as a targetable vulnerability in hypoxic solid tumors, Sci. Adv. 7 (35) (2021) eabj0364.
[48] H.T. Endale, W. Tesfaye, T.A. Mengstie, ROS induced lipid peroxidation and their role in ferroptosis, Front. Cell Dev. Biol. 11 (2023) 1226044.
[49] X. Yin, B. Tang, J.H. Li, et al., ID1 promotes hepatocellular carcinoma proliferation and confers chemoresistance to oxaliplatin by activating pentose phosphate pathway, J. Exp. Clin. Cancer Res. 36 (1) (2017) 166.
[50] L. Ma, A. Xu, L. Kang, et al., LSD1-Demethylated LINC01134 confers oxaliplatin resistance through SP1-induced p62 transcription in HCC, Hepatology 74 (6) (2021) 3213–3234.
[51] J. Mei, W. Lin, S. Li, et al., Long noncoding RNA TINCR facilitates hepatocellular carcinoma progression and dampens chemosensitivity to oxaliplatin by regulating the miR-195-3p/ST6GAL1/NF-κB pathway, J. Exp. Clin. Cancer Res. 41 (1) (2022) 5.
[52] X. Qu, B. Liu, L. Wang, et al., Loss of cancer-associated fibroblast-derived exosomal DACT3-AS1 promotes malignant transformation and ferroptosis-mediated oxaliplatin resistance in gastric cancer, Drug Resist. Updates 68 (2023) 100936.
[53] Q. Zhang, T. Deng, H. Zhang, et al., Adipocyte-derived exosomal MTTP suppresses ferroptosis and promotes chemoresistance in colorectal cancer, Adv. Sci. 9 (28) (2022) e2203357.
[54] M. Zhan, Y. Ding, S. Huang, et al., Lysyl oxidase-like 3 restrains mitochondrial ferroptosis to promote liver cancer chemoresistance by stabilizing dihydroorotate dehydrogenase, Nat. Commun. 14 (1) (2023) 3123.